



1 Concentrations and radiative forcing of anthropogenic aerosols from 1750-2014
2 simulated with the OsloCTM3 and CEDS emission inventory

3

4 Marianne T. Lund^{1*}, Gunnar Myhre¹, Amund S. Haslerud¹, Ragnhild B. Skeie¹, Jan Griesfeller²,
5 Stephen M. Platt³, Rajesh Kumar^{4,5}, Cathrine Lund Myhre³, Michael Schulz²

6

7 *1 CICERO Center for International Climate Research, Oslo, Norway*

8 *2 Norwegian Meteorological Institute, Oslo, Norway*

9 *3 NILU – Norsk institutt for luftforskning, Dept. Atmospheric and Climate Research (ATMOS),*
10 *Kjeller, Norway*

11 *4 Advanced Study Program, National Center for Atmospheric Research, Boulder, Colorado, USA*

12 *5 Atmospheric Chemistry Division, National Center for Atmospheric Research, Boulder, Colorado,*
13 *USA*

14

15 *Corresponding author: m.t.lund@cicero.oslo.no

16

17

18

19

20

21

22

23

24

25

26

27



28 Abstract

29

30 We document the ability of the new generation Oslo chemistry-transport model, OsloCTM3, to
31 accurately simulate present-day aerosol distributions. The model is then used with the new
32 Community Emission Data System (CEDS) historical emission inventory to provide updated time
33 series of anthropogenic aerosol concentrations and consequent direct radiative forcing (RFari)
34 from 1750 to 2014.

35 Overall, the OsloCTM3 performs well compared with measurements of surface concentrations and
36 remotely sensed aerosol optical depth. Concentrations are underestimated in Asia, but the higher
37 emissions in CEDS than previous inventories result in improvements compared to observations.
38 The black carbon (BC) treatment in OsloCTM3 gives better agreement with observed vertical BC
39 profiles relative to the predecessor OsloCTM2. However, Arctic wintertime BC concentrations
40 remain underestimated, and a range of sensitivity tests indicate that better physical understanding
41 of processes associated with atmospheric BC processing is required to simultaneously reproduce
42 both the observed features. Uncertainties in model input data, resolution and scavenging affects
43 the distribution of all aerosols species, especially at high latitudes and altitudes. However, we find
44 no evidence of consistently better model performance across all observables and regions in the
45 sensitivity tests than in the baseline configuration.

46 Using CEDS, we estimate a total net RFari in 2014 relative to 1750 of -0.17 W m^{-2} , significantly
47 weaker than the IPCC AR5 2010-1750 estimate. Differences are attributable to several factors,
48 including stronger absorption by organic aerosol, updated parameterization of BC absorption, and
49 reduced sulfate cooling. The trend towards a weaker RFari over recent years is more pronounced
50 than in the IPCC AR5, illustrating the importance of capturing recent regional emission changes.

51

52

53

54

55

56

57

58

59



60

61

62 1 Introduction

63

64 Changes in anthropogenic emissions over the industrial period have significantly altered the
65 abundance, composition and properties of atmospheric aerosols, causing a change in the radiative
66 energy balance. The net energy balance change is determined by a complex interplay of different
67 types of aerosols and their interactions with radiation and clouds, causing both positive (warming)
68 and negative (cooling) radiative impacts. Global aerosols were estimated by the Intergovernmental
69 Panel on Climate Change fifth assessment report (IPCC AR5) to have caused a total effective
70 radiative forcing (ERF) of -0.9 W m^{-2} over the industrial era from 1750 to 2011, but with
71 considerable uncertainty (-1.9 to -0.1 W m^{-2}) [Boucher *et al.*, 2013].

72 This large uncertainty range arises from a number of factors, including uncertainties in emissions
73 and atmospheric aerosol distributions. Historical emission estimates for anthropogenic aerosol and
74 precursor compounds are key data needed for climate and atmospheric chemistry transport models
75 in order to examine how these drivers have contributed to climate change. The historical emission
76 data set used in the Coupled Model Intercomparison Project Phase 5 (CMIP5), important for the
77 IPCC AR5 forcing estimates, covered the period up to 2000. The Community Emissions Data
78 System (CEDS) recently published a new time series of emissions from 1750 to 2014, which will
79 be used in the upcoming CMIP6. CEDS includes several improvements over previous inventories,
80 including annual temporal resolution with seasonal cycles, consistent methodology between
81 different species, and extending the time series to more recent years [Hoesly *et al.*, 2018]. During
82 the period from 2000 to 2014, global emissions of black carbon (BC) and organic carbon (OC)
83 have increased, while nitrogen oxide (NO_x) emissions have been relatively constant after 2008,
84 and sulfur dioxide (SO₂) emissions were back at 2000 levels in 2014, after a temporary increase
85 [Hoesly *et al.*, 2018]. Furthermore, both CEDS and other recent emission inventories report
86 considerably higher estimates of global BC and OC emissions in recent years than earlier
87 inventories [Granier *et al.*, 2011; Klimont *et al.*, 2017; Lamarque *et al.*, 2010; Wang *et al.*, 2014].
88 The global trend in emissions is driven by a strong increase in emissions from Asia and Africa,
89 and a decline in North America and Europe. Capturing such geographical differences is essential,
90 as the distribution, lifetime and radiative forcing of aerosols depend on their location.

91 The diversity in radiative forcing (RF) estimates also stems from uncertainties in the simulated
92 spatiotemporal distribution of aerosols, their chemical composition and properties. After emission
93 or formation, particles undergo transport, mixing, chemical aging and removal by dry and wet
94 deposition, resulting in a short atmospheric lifetime, and a highly heterogeneous distribution in
95 space and time. Consequently, accurate representation of the observed aerosol distributions
96 remains challenging. Previous studies have shown that considerable diversity exist between global
97 models. Bian *et al.* [2017] found that the atmospheric burden of nitrate aerosols differ by a factor
98 of 13 between the models in AeroCom Phase III, caused by differences in both chemical and



99 deposition processes. A smaller, but still considerable, model spread in the simulated burden of
100 organic aerosols (OA) from 0.6-3.8 Tg was found by *Tsigaridis et al.* [2014]. It was also shown
101 that OA concentrations on average were underestimated. There has been particular focus on BC
102 aerosols over recent years. Multi-model studies have shown variations in global BC burden and
103 lifetime up to a factor of 4-5 [*Lee et al.*, 2013; *Samset et al.*, 2014]. Previous comparisons of
104 modeled BC distributions with observations have also pointed to two distinct features common to
105 many models: an overestimation of high altitude concentrations at low- to mid-latitudes and
106 discrepancies in the magnitude and seasonal cycle of high-latitude surface concentrations (e.g.,
107 [*Eckhardt et al.*, 2015; *Lee et al.*, 2013; *Samset et al.*, 2014; *Schwarz et al.*, 2013]).

108 Changes to one or more of the abovementioned processes may have considerable impact on the
109 simulated concentrations, and propagates to uncertainties in estimates of both RF and climate
110 impact. A number of recent studies have investigated possible factors controlling the BC
111 distribution, focusing on aging and wet scavenging processes (e.g., [*Bourgeois and Bey*, 2011;
112 *Browse et al.*, 2012; *Fan et al.*, 2012; *Hodnebrog et al.*, 2014; *Kipling et al.*, 2013; *Lund et al.*,
113 2017; *Mahmood et al.*, 2016]), resulting in notable improvements, at least for specific regions or
114 observational data sets. With a few notable exceptions (e.g., [*Kipling et al.*, 2016]), fewer studies
115 have focused on a broader set of aerosol species or the combined impact in terms of total aerosol
116 optical depth (AOD).

117 Here we use the CEDS historical emission inventory as input to the chemistry-transport model
118 OsloCTM3 to quantify the change in atmospheric concentrations over the period of 1750 to 2014.
119 The OsloCTM3 is an update of the OsloCTM2, and includes several key changes compared to its
120 predecessor. The significant existing model spread and sensitivity to process parameterizations
121 underlines the need for careful and updated documentation of new model versions, and the
122 increasing amount of available measurement data allows for improved evaluation. Before the
123 model is used to quantify historical time series, we therefore evaluate the simulated present-day
124 aerosol concentrations and optical depth against a range of observations. To get a first-order
125 overview of how uncertainties in key processes and parameters affect the atmospheric abundance
126 and distribution of aerosols in the OsloCTM3, we perform a range of sensitivity simulations. In
127 addition to changes in the scavenging (solubility) assumptions, runs are performed with different
128 emission inventories, horizontal resolution, and meteorological data. The impact on individual
129 species and total AOD, as well as on the model performance compared with observations, is
130 investigated. Finally, we present updated estimates of the historical evolution of radiative forcing
131 due to aerosol-radiation interactions from pre-industrial to present, taking into account recent
132 literature on aerosol optical properties. Section 2 describes the model and methods, while results
133 are presented in Sect. 3 and discussed in Sect. 4. The conclusions are given in Sect. 5.

134

135 2 Methods

136



137 2.1 OsloCTM3

138

139 The OsloCTM3 is a global 3-dimensional chemistry-transport model driven by 3-hourly
140 meteorological forecast data [Søvde *et al.*, 2012]. The OsloCTM3 has evolved from its predecessor
141 OsloCTM2 and includes several updates to the convection, advection, photodissociation and
142 scavenging schemes. Compared with OsloCTM2, the OsloCTM3 has a faster transport scheme, an
143 improved wet scavenging scheme for large scale precipitation, updated photolysis rates and a new
144 lightning parameterization. The main updates and subsequent effects on gas-phase chemistry were
145 described in detail in Søvde *et al.* [2012]. Here we document the aerosols in OsloCTM3, including
146 BC, primary and secondary organic aerosols (POA, SOA), sulfate, nitrate, dust and sea salt. The
147 aerosol modules in OsloCTM3 are generally inherited and updated from OsloCTM2. The
148 following paragraph briefly describes the parameterizations, including updates new to this work.

149

150 The carbonaceous aerosol module was first introduced by *Berntsen et al.* [2006] and has later been
151 updated with snow deposition diagnostics [*Skeie et al.*, 2011]. The module is a bulk scheme, with
152 aerosols characterized by total mass and aging represented by transfer from hydrophobic to
153 hydrophilic mode at a constant rate. In the early model versions, this constant rate was given by a
154 global exponential decay of 1.15 days. More recently, latitudinal and seasonal variation in transfer
155 rates based on simulations with the microphysical aerosol parameterization M7 were included
156 [*Lund and Berntsen*, 2012; *Skeie et al.*, 2011]. Previous to this study, additional M7 simulations
157 have been performed to include a finer spatial and temporal resolution in these transfer rates. In
158 OsloCTM3 the carbonaceous aerosols from fossil fuel and biofuel combustion are treated
159 separately, allowing us to capture differences in optical properties in subsequent radiative transfer
160 calculations (Sect. 2.4). In contrast to the OsloCTM2, OsloCTM3 treats organic matter (OM)
161 instead of OC. If emissions are given as OC, a factor of 1.6 for anthropogenic emissions and 2.6
162 for biomass burning sources is used for the OC-to-OM conversion. Upon emission, 20% of BC is
163 assumed to be hydrophilic and 80% hydrophobic, while a 50/50 split is assumed for OM. An
164 additional update in this work is the inclusion of marine primary organic aerosols following the
165 methodology by *Gantt et al.* [2015], where emissions are determined by production of sea spray
166 aerosols and oceanic chlorophyll A. Monthly concentrations of chlorophyll A from the same year
167 as the meteorological data is taken from the Moderate Resolution Imaging Spectroradiometer
168 (MODIS; available from https://modis.gsfc.nasa.gov/data/dataproduct/chlor_a.php), while sea spray
169 aerosols are simulated by the OsloCTM3 sea salt module. The climatological annual mean total
170 emission of marine OM is scaled to 6.3 Tg based on *Gantt et al.* [2015].

171 The formation, transport and deposition of SOA are parameterized as described by *Hoyle et al.*
172 [2007]. A two product model (*Hoffmann et al.*, 1997) is used to represent the oxidation products
173 of the precursor hydrocarbons and their aerosol forming properties. Precursor hydrocarbons which
174 are oxidized to form condensable species include both biogenic species such as terpenes and
175 isoprene, as well as species emitted predominantly by anthropogenic activities (toluene, m-xylene,



176 methylbenzene and other aromatics). The gas/aerosol partitioning of semi-volatile inorganic
177 aerosols is treated with a thermodynamic model [Myhre *et al.*, 2006]. The chemical equilibrium
178 between inorganic species (ammonium, sodium, sulfate, nitrate and chlorine) is simulated with the
179 Equilibrium Simplified Aerosol model (EQSAM) [Metzger *et al.*, 2002a; Metzger *et al.*, 2002b].
180 The aerosols are assumed to be metastable, internally mixed and obey thermodynamic gas/aerosol
181 equilibrium. Nitrate and ammonium aerosols are represented by a fine mode, associated with sulfur,
182 and a coarse mode associated with sea salt, and it is assumed that sulfate and sea salt do not interact
183 through chemical equilibrium [Myhre *et al.*, 2006]. The sulfur cycle chemistry scheme and
184 aqueous-phase oxidation is described by Berglen *et al.* [2004].

185

186 The sea salt module originally introduced by Grini *et al.* [2002] has been updated with a new
187 production parameterization following recommendations by Witek *et al.* [2016]. Using satellite
188 retrievals, Witek *et al.* (2016) evaluated different sea spray aerosol emission parametrizations and
189 found the best agreement with the emission function from Sofiev *et al.* [2011] including the sea
190 surface temperature adjustment from Jaeglé *et al.* [2011]. Compared to the previous scheme, the
191 global production of sea salt is reduced, while there is an increase in the tropics. This will have an
192 impact on the uptake of nitric acid in sea salt particles, consequently affecting NO_x, hydroxide
193 (OH) and ozone levels. However, here we limit the scope to aerosols. The Dust Entrainment and
194 Deposition (DEAD) model v1.3 was implemented into OsloCTM2 by Grini *et al.* [2005] and is
195 also used in OsloCTM3. As a minor update, the DEAD energy budget calculation now uses
196 radiative surface properties and soil moisture from the meteorological fields.

197

198 Wet scavenging of aerosols is calculated based on European Center for Medium-Range Weather
199 Forecast (ECMWF) data for convective activity, cloud fraction and rain fall, and on the solubility
200 of individual species. For large-scale precipitation, OsloCTM3 has a more complex cloud model
201 that accounts for overlapping clouds and rain (Neu and Prather 2012). Convective scavenging is
202 based on the Tiedtke mass flux scheme (Tiedtke 1989) and is unchanged from the OsloCTM2. The
203 solubility of aerosols is given by constant fractions, given for each species and type of precipitation
204 (i.e., large-scale rain, large-scale ice, and convective) (Table 2). Dry deposition rates are
205 unchanged from OsloCTM2, but the OsloCTM3 includes a more detailed land use dataset (18 land
206 surface categories at 1°x1° horizontal resolution compared to 5 categories at T42 resolution),
207 which affects the weighting of deposition rates for different vegetation categories.

208

209

210 2.2 Emissions

211

212 The baseline and historical simulations use the CEDS anthropogenic [Hoesly *et al.*, 2018; Smith *et al.*
213 *et al.*, 2015] and biomass burning (BB4CMIP) [van Marle *et al.*, 2017] emissions. The CEDS
214 inventory provide monthly gridded emissions of climate-relevant greenhouse gases, aerosols and
215 precursor species from 1750 to 2014 using a consistent methodology over time. Anthropogenic



216 CEDS emissions are comparable to, but generally higher than, other existing inventories [*Hoesly*
217 *et al.*, 2018]. Biogenic emissions are from the inventory developed with the Model of Emissions
218 of Gases and Aerosols from Nature under the Monitoring Atmospheric Composition and Climate
219 project (MEGAN-MACC) [*Sindelarova et al.*, 2014] and are held constant at the year 2010 level.
220 Here we use the CEDS version released in 2016 (hereafter CEDSv16). In May 2017, after
221 completion of our historical simulations, an updated version of the CEDS emission inventory was
222 released after users reported year-to-year inconsistencies in the country/sector level gridded data.
223 The emission totals were not affected, but there were occasional shifts in the distribution within
224 countries (<http://www.globalchange.umd.edu/ceds/ceds-cmip6-data/>). The potential implications
225 for our simulations are discussed below.

226 Two other emission inventories are also used. The ECLIPSEv5 emission dataset was created with
227 the Greenhouse Gas - Air Pollution Interactions and Synergies (GAINS) model [*Amann et al.*,
228 2011] and provides emissions in 5 year intervals from 1990 to 2015, as well as projections to 2050
229 [*Klimont et al.*, 2017]. The 1990-2015 emission series was recently used to simulate changes in
230 aerosols and ozone and their RF [*Myhre et al.*, 2017]. Here we only use emissions for 2010 in the
231 sensitivity simulation.

232 The Representative Concentration Pathways (RCPs) [*van Vuuren et al.*, 2011] were developed as
233 a basis for near- and long-term climate modeling and were used in CMIP5 and Atmospheric
234 Chemistry and Climate Model Intercomparison Project (ACCMIP) experiments. While the four
235 RCPs span a large range in year 2100 RF, emissions of most species have not diverged
236 significantly in 2010 and we select the RCP4.5 for use here [*Thomson et al.*, 2011]. Table S1
237 summarized total global emissions of BC, OC, NO_x and SO₂ in 2010 in each of the three scenarios.

238 In the simulations with the ECLIPSEv5 and RCP4.5 inventories, biomass burning emissions are
239 from the Global Fire Emission Database Version 4 (GFED4) [*Randerson et al.*, 2017]. The
240 BB4CMIP emissions are constructed with GFED4 1997-2015 emissions as a basis [*van Marle et al.*,
241 2017] and emissions in 2010 are similar in both datasets. Hence, any difference between the
242 sensitivity simulations stems from differences in the anthropogenic inventory.

243

244

245 2.3 Simulations

246

247 Time slice simulations with CEDSv16 emissions for 1750, 1850 and from 1900 to 2014 are
248 performed (every ten years from 1900-1980, thereafter every five years), including six months
249 spin-up. The model is run with year 2010 meteorological data and a horizontal resolution of
250 2.25x2.25 degrees (denoted 2x2), with 60 vertical layers. While *Søvde et al.* [2012] used
251 meteorological data from the ECMWF IFS model cycle 36r1, we apply here meteorology from the
252 ECMWF OpenIFS cycle 38r1 (<https://software.ecmwf.int/wiki/display/OIFS/>).

253



254 Additional model runs are performed to investigate the importance of differences in key processes
255 for the aerosol distributions and model performance (Table 1). In addition to the CEDSv16
256 emissions, the model is run with ECLIPSEv5 and RCP4.5 emission inventories for anthropogenic
257 emissions and GFEDv4 biomass burning emissions. Additionally, we perform simulations with
258 1.125x1.125 degrees (denoted 1x1) horizontal resolution. To investigate the importance of
259 meteorology, the simulation with CEDSv16 emissions is repeated with meteorological data for
260 year 2000 instead of 2010. Year 2000 is selected due to its opposite El Niño–Southern Oscillation
261 (ENSO) index compared to 2010. Finally, three model runs are performed with increased and
262 decreased scavenging efficiency by large-scale ice clouds and decreased aerosol scavenging by
263 liquid (large-scale and convective) precipitation. The efficiency with which aerosols are scavenged
264 by precipitation is determined by a fixed fraction representing the fraction of the grid box that is
265 available for removal, while the rest is assumed to be hydrophobic. Table 2 summarizes the
266 fractions in the baseline configuration and the assumptions in the three sensitivity tests.
267

268 2.4 Radiative transfer

269

270 We calculate the radiative forcing of anthropogenic aerosols due to aerosol-radiation interactions
271 (RFari) [Myhre *et al.*, 2013b]). The radiative transfer calculations are performed with a multi-
272 stream model using the discrete ordinate method [Stamnes *et al.*, 1988]. The model includes gas
273 absorption, Rayleigh scattering, absorption and scattering by aerosols, and scattering by clouds.
274 The aerosol optical properties have been updated from earlier calculations using this radiative
275 transfer model [Myhre *et al.*, 2007; Myhre *et al.*, 2009], in particular those associated with aerosol
276 absorption. The Bond and Bergstrom [2006] recommendation of a mass absorption coefficient
277 (MAC) for BC of around $7.5 \text{ m}^2 \text{ g}^{-1}$ for freshly emitted BC and an enhancement factor of 1.5 for
278 aged BC was used previously. In the present analysis, we apply a parametrization of MAC from
279 observations over Europe [Zanatta *et al.*, 2016], where MAC depends on the ratio of non-BC to
280 BC abundance. The mean MAC of BC from the observations over Europe is around $10 \text{ m}^2 \text{ g}^{-1}$ at
281 630 nm [Zanatta *et al.*, 2016]. For low aerosol concentrations we apply the approach from Bond
282 and Bergstrom [2006]. The absorption by organic matter is uncertain [Bond *et al.*, 2013]. Here, we
283 have implemented absorbing organic matter according to refractive indices from Kirchstetter *et al.*
284 [2004] to 1/3 of the biofuel organic matter and 1/2 of the SOA from anthropogenic volatile organic
285 carbon (VOC) precursors. The remaining fractions of biofuel, fossil fuel and marine POA and
286 SOA (anthropogenic and all natural VOCs) are assumed to be purely scattering organic matter.
287

288 2.5 Observations

289

290 A range of observational datasets are used to evaluate the model performance in the baseline
291 simulation. Note that we use the term “black carbon” in a qualitative manner throughout the
292 manuscript to refer to light-absorbing carbonaceous aerosols. However, when comparing with
293 measurements, we use either elemental carbon (EC) or refractive BC (rBC), depending on whether



294 the data is derived from methods specific to the carbon content of carbonaceous aerosols or
295 incandescence methods, in line with recommendations from *Petzold et al.* [2013].
296 Measured surface concentrations of EC, OC, sulfate and nitrate are obtained from various
297 frameworks. For the US, measurements from IMPROVE (Interagency Monitoring of Protected
298 Visual Environments) and CASTNET (Clean Air Status and Trends Network) are used. For
299 Europe, data from EMEP (European Monitoring and Evaluation Programme) [*Tørseth et al.*, 2012]
300 and ACTRIS (Aerosols, Clouds and Trace gases Research InfraStructure) [*Cavalli et al.*, 2016;
301 *Putaud et al.*, 2010] is used. EMEP and ACTRIS sites are all regional background sites,
302 representative for a larger area. To broaden the geographical coverage we also compare the model
303 output against additional observations from the CMA Atmospheric Watch Network (CAWNET)
304 in China [*Zhang et al.*, 2012] and those reported in the literature from India (see *Kumar et al.* [2015]
305 for more details). CASTNET, IMPROVE, EMEP and ACTRIS data is from year 2010, while
306 CAWNET observations were sampled in 2006-2007 and the observational data base from India
307 compiled by *Kumar et al.* [2015] cover a range of years. IMPROVE provides mass of aerosols
308 using filter analysis of measurements of particulate matter with diameter of less than 2.5
309 micrometers (PM_{2.5}), while CASTNET uses an open-face filter pack system with no size restriction
310 to measure concentrations of atmospheric sulfur and nitrogen species [*Lavery et al.*, 2009]. Mass
311 of individual species from the CAWNET network is obtained from aerosol chemical composition
312 analysis performed on PM₁₀ samples [*Zhang et al.*, 2012]. EMEP and ACTRIS measurements of
313 EC and OC are in the PM_{2.5} range, whereas nitrate and sulfate measurements are filter-based with
314 no size cutoff limit. Data resulting from EMEP and ACTRIS are archived in the EBAS data base
315 (<http://ebas.nilu.no>) at NILU - Norwegian Institute for Air Research, and are openly available (see
316 also Data availability).
317
318 Modeled AOD is evaluated against the Aerosol Robotics Network (AERONET). AERONET is a
319 global network of stations measuring radiance at a range of wavelengths with ground-based sun-
320 photometers, from which aerosol column burden and optical properties can be retrieved [*Dubovik*
321 *and King*, 2000; *Holben et al.*, 1998]. The AERONET data was processed through the validation
322 tools available from the AeroCom data base hosted by Met Norway
323 (<http://aerocom.met.no/data.html>). We also compare against AOD retrievals from MODIS-Aqua
324 and Terra (level 3 atmosphere products, AOD550 combined dark target and deep blue, product
325 version 6) [*MOD08*, 2018] and the Multi-angle Imaging SpectroRadiometer (MISR) (level 2
326 aerosol product, product version 4) [*MISR*, 2018].
327
328 Figure S1 depicts the locations of all the stations. For comparison with surface concentrations and
329 AERONET AOD, the model data is linearly interpolated to the location of each station using
330 monthly mean or 3-hourly output. In the case of AERONET, high mountain stations (here defined
331 as having an elevation higher than 1000 meter above sea level) are excluded following *Kinne et*
332 *al.* [2013]. For comparison with observed OC surface concentrations, modeled OA is converted to
333 OC using factor of 1.6 for POA and 1.8 for SOA. Unless measurements are restricted to the PM_{2.5}
334 size range, the comparison includes both fine and coarse mode modeled nitrate (Sect. 2.1). Several



335 statistical metrics are used to assess the model skill, including correlation coefficient (R), root
336 mean square error (RMSE), variance and normalized mean bias (NMB).

337 The modeled vertical distribution of BC is compared with aircraft measurements of refractory BC
338 (rBC) from the HIAPER Pole-to-Pole Observations (HIPPO) campaign [Wofsy *et al.*, 2011].
339 Vertical profiles of BC from OsloCTM2 have been evaluated in several previous studies (e.g.,
340 Samset *et al.* [2014]) and a more thorough comparison of OsloCTM3 results against a broader set
341 of campaigns is provided by Lund *et al.* [2018]. In the present analysis we focus on data from the
342 third phase (HIPPO3) flights, the only phase that was conducted in 2010, i.e., the same year as our
343 sensitivity simulations. Model data is extracted along the flight track using an online flight
344 simulator. The data is separated into five latitude regions and vertical profiles constructed by
345 averaging observations and model output in 13 altitude bins.

346

347 3 Results

348

349 We first document the aerosol distributions simulated in the baseline model configuration,
350 focusing on the anthropogenic contribution, and compare with observations, multi-model studies
351 and results from the sensitivity tests. With the present-day model performance evaluated, we then
352 present the updated historical development of RFari of anthropogenic aerosols.

353

354 3.1 Evaluation of present-day aerosol distributions

355

356 The global mean aerosol burdens in the baseline simulation are summarized in Table 3 (top row),
357 with spatial distribution shown in Fig. S2. Table S3 also shows the split of OA between secondary
358 and primary sources. Compared to results from the AeroCom III experiment, the OsloCTM3
359 sulfate burden of 5.4 mg m⁻² estimated here is about 50% higher than the multi-model mean of 3.5
360 mg m⁻² and 35% higher than OsloCTM2 [Bian *et al.*, 2017]. The nitrate burden is nearly a factor
361 three higher than both the AeroCom multi-model mean and OsloCTM2 burden, and higher than
362 all nine models contributing in AeroCom III [Bian *et al.*, 2017]. This is mainly due to a higher
363 burden of coarse mode nitrate aerosols, associated with less efficient scavenging of sea salt in
364 OsloCTM3 than OsloCTM2. The global budgets of OA simulated by the AeroCom II models was
365 analyzed by Tsigaridis *et al.* [2014]. The burden of OA in the OsloCTM3 of 3.4 mg m⁻² is close
366 to their multi-model mean of 3.1 mg m⁻² and 25% higher than the OsloCTM2. The OsloCTM3
367 estimate includes the contribution from marine OA emissions (Sect. 2.1). This was included in
368 only some of the AeroCom II models and not in OsloCTM2, which may partly explain the slightly
369 lower OsloCTM2 OA burden in Tsigaridis *et al.* [2014]. However, the marine POA only
370 contributes around 3% to the total OA (Table S3). The global BC burden of 0.23 mg m⁻² is also
371 close to the mean of the AeroCom II models of 0.25 mg m⁻² [Samset *et al.*, 2014]. We note that
372 different emission inventories were used in the AeroCom experiments and the present analysis,



373 however, the comparison shows that the aerosol burdens simulated by OsloCTM3 fall within the
374 range of existing estimates from global models.

375

376 Figure 1 shows annual mean measured surface concentrations of EC, OC, sulfate and nitrate in
377 Europe, North America and Asia against output from the baseline OsloCTM3 simulation. Overall,
378 the OsloCTM3 shows a high correlation of 0.8-0.9 with measured surface concentrations. There
379 is a general tendency of underestimation by the model, with the lowest NMB and RMSE for BC
380 and nitrate (-23%) and the highest for sulfate (-52%). There are, however, notable differences in
381 model performance between data sets in different regions, as seen from Table S2. For all species,
382 the NMB and RMSE are highest for measurements in China. For instance, excluding the
383 CAWNET measurements, reduces the NMB for sulfate in Fig. 1 from -52% to -31% (not shown).
384 In contrast, the correlation is generally similar to, or higher than, other regions. In the case of BC
385 and nitrate, the model slightly overestimates concentrations in Europe and North America, but
386 underestimates Asian measurements. The best overall agreement is generally with IMPROVE
387 observations in North America. Differences in instrumentation between different networks can
388 affect the evaluation. *Lavery et al.* [2009] found that measurements from CASTNET typically gave
389 higher nitrate surface concentrations than values obtained from co-located IMPROVE stations,
390 which could partly explain the NMB of opposite sign in these two networks in Table S2. For BC,
391 we also include measurements from across India compiled by *Kumar et al.* [2015]. This is a region
392 where emissions have increased strongly, but where evaluation of the model performance so far
393 has been limited due to availability of observations. The model underestimates concentrations with
394 a NMB of -43%, however, the correlation of 0.60 is similar to the comparison with data from
395 China and higher than the other regions. An examination of the monthly concentrations (Fig. S3)
396 shows that the largest discrepancies occur during winter, with the largest bias found for
397 measurements in North East India. One possible reason could be missing or underestimated
398 emission sources. This finding is similar to the comparison of measurements against WRF-chem
399 by *Kumar et al.* [2015]. The seasonality of BC concentrations has also been an issue at high
400 northern latitudes, where earlier versions of the OsloCTM strongly underestimated winter and
401 springtime surface concentrations at Arctic stations [*Lund et al.*, 2017; *Skeie et al.*, 2011], similar
402 to many other models [*Eckhardt et al.*, 2015]. This Arctic underestimation persists in the current
403 version of the model. Seasonal differences exist also in other regions, but not consistently across
404 measurement networks. Compared with EC measurements from EMEP/ACTRIS the correlation
405 is poorer during winter and spring, and the model underestimate concentrations in contrast to a
406 positive NMB in summer and fall. However, due to the relatively low number of stations, these
407 values are sensitive to a few stations with larger measurement-model discrepancies. For both
408 IMPROVE and EMEP/ACTRIS, the model underestimation of sulfate is larger during summer
409 and fall, but with opposite seasonal differences in correlation. In general, the number of stations
410 and evaluation of data from only one year limits the analysis of seasonal variations.

411 We do not evaluate ammonium concentrations in the present analysis, as that requires a detailed
412 discussion of the nitrate and sulfate budgets, which has been covered by the recent multi-model



413 nitrate evaluation study by *Bian et al.* [2017], in which the OsloCTM3 participated. Results
414 showed that the OsloCTM3 is close to the multi-model mean and similar to the other models in
415 terms of agreement with observed ammonium concentrations across USA, Europe and East Asia,
416 with an average correlation of 0.47.

417 In May 2017, after completion of our historical simulations, an updated version of the CEDS
418 emission inventory was released after an error in the code was reported (see Sect. 2.2). This
419 resulted in occasional shifts in the spatial distribution of emissions within countries with large
420 spatial extent (e.g., USA and China). Since the emission totals were not affected, the impact on
421 our RFari estimates is likely to be small, but shifts in the emission distribution could impact the
422 model evaluation, in particular for surface concentrations. While repeating all simulations require
423 more resources than available to us, we have performed a limited investigation for the US, which
424 is one of the regions affected by the emission distribution bug (Fig. S4a). We limit the analysis to
425 BC, using a model data from one year, but note that emissions of other species are also affected.
426 The comparison against measurements from the IMPROVE network (Fig. S4b-d) shows an
427 increase in correlation from 0.33 to 0.43 and a 25 percent reduction in the RMSE when using the
428 May 2017 version of emissions.

429 As shown in Table S2, the model overestimate surface concentrations in some regions and
430 underestimate them in others. Compensating biases can influence the evaluation of total AOD.
431 Moreover, the biases differ in magnitude between different species. Moving one step further, we
432 therefore examine the average aerosol composition in the three regions where this is possible with
433 our available measurements. Figure 2 shows the relative contribution from different aerosols
434 species to the total mass in the IMPROVE, EMEP, ACTRIS and CAWNET measurements and the
435 corresponding model results. The number of available aerosol species varies between the
436 measurement networks and we include sea salt from IMPROVE and ammonium from CAWNET.
437 Additionally, the number of stations where simultaneous measurements of all species were
438 available also differ substantially, with 16 for CAWNET, 5 for EMEP/ACTRIS and 172 for
439 IMPROVE. Overall, the relative composition is well represented by the model. The agreement is
440 particularly good for the IMPROVE network. Compared to measurements from CAWNET, the
441 model has a lower relative contribution from OC and more sulfate. In the case of Europe, nitrate
442 aerosols also constitute a significantly larger fraction in the model than in the observations. The
443 evaluation of nitrate is complicated by possible differences in the detection range of
444 instrumentation compared to the size of the two nitrate modes in the model (Sect. 2.1). The
445 comparison against EMEP nitrate data includes both coarse and fine mode modeled nitrate.
446 Excluding the coarse mode, the fraction of total mass attributable to nitrate decreases from 43% to
447 28%, which is much closer to the observed 30% contribution. However, this affects the comparison
448 in Figure 1, resulting in a negative NMB of -34%, compared to -23% when including both coarse
449 and fine mode. This suggest that part, but not all, of the nitrate represented as a coarse mode in the
450 model is measured by the instrument, pointing to a need for a more sophisticated size distribution



451 in the model to make better use of available observations. The low number of available stations
452 from EBAS could also an important factor.

453 Next, we examine total AOD. Figure 3 shows modeled AOD and aerosol absorption optical depth
454 (AAOD), AOD retrieved from MODIS-Aqua and comparison of modeled AOD with AERONET
455 observations. Modeled global, annual mean AOD and AAOD is 0.13 (Fig. 3a) and 0.0051 (Fig.
456 3b), respectively. The overall spatial pattern of modeled AOD agrees well with MODIS (Fig. 3c),
457 however, the latter gives a higher global mean of 0.16 and clearly higher values in North India and
458 parts of China, as well as Central Africa. These peak values are similar to MODIS-Terra, but less
459 pronounced in the AOD retrieved from MISR (Fig. S5), illustrating important differences between
460 different remote sensing products. Nevertheless, an underestimation of modeled AOD in Asia is
461 consistent with results from the evaluation of surface concentrations and can also be seen in the
462 comparison against AERONET, as discussed below. The OsloCTM3 shows a good agreement
463 with measured AOD from the AERONET network, with an overall correlation of 0.82 and RMSE
464 of 0.11, when using monthly mean data from 266 stations (Fig. 3d). Note that the modeled global
465 mean AOD is 0.13, but the model mean at the AERONET stations is 0.175 (Fig 3d) and has only
466 a NMB of -11.8%. Many of the AERONET stations tend not to be regional background sites, but
467 can be influenced by local pollution (e.g., Wang *et al.* [2018])

468 However, as for surface concentrations, there are notable regional differences. Fig. S6 compares
469 modeled AOD against AERONET stations in Europe, North America, India and China separately.
470 The best agreement is found for Europe and North America, with NMB of -0.4% and -13%,
471 respectively, and RMSE of approx. 0.05. The correlation is higher for North America (0.71) than
472 Europe (0.63). A relatively high correlation of 0.71 is also found for stations in China. However,
473 the NMB and RMSE is higher (-34.5% and 0.25). There are significantly fewer observations for
474 comparison with modeled AOD over India, but the ones available give NMB and RMSE on the
475 same order of magnitude as for China, but a lower correlation (0.45).

476 Ground-based measurements can also provide information about column absorption aerosol
477 optical depth (AAOD). Such information has been used to constrain the absorption of BC and
478 provide top-down estimate of the direct BC RF (e.g., [Bond *et al.*, 2013]). However, retrieval and
479 application of AERONET AAOD is associated with a number of challenges and uncertainties (e.g.,
480 [Samset *et al.*, 2018]), hence such an evaluation is not performed here.

481 Recent literature has pointed to important representativeness errors arising when constraining
482 models using observations due to the coarse spatial and temporal scales of global models compared
483 with the heterogeneity of observations. Schutgens *et al.* [2016a] found differences in RMSE of up
484 to 100% for aerosol optical thickness when aggregating high resolution model output over grid
485 boxes representative of the resolution of current global models compared to small areas
486 corresponding to satellite pixels. Smaller, but notable, differences of up to 20% were found when
487 monthly mean model data was used, as in the present analysis. However, that did not account for
488 issues related to temporal collocation, which can also introduce considerable errors [Schutgens *et*



489 *al.*, 2016b]. In a recent study, Wang *et al.* [2018] found a spatial representativeness error of 30%
490 when constraining AAOD modeled at a $2^\circ \times 2^\circ$ horizontal resolution against AERONET retrievals.
491 However, further work is needed to investigate whether similar biases exist for AOD.

492

493 3.2 Sensitivity of aerosols distributions to model input and process parameterization

494

495 As shown in the section above, the OsloCTM3 performs well compared against observed AOD.
496 Still, a number of factors influence the simulated distributions of individual aerosol species. To
497 assess the importance of key uncertainties for modeled distributions and model performance, we
498 perform a range of sensitivity simulations to examine the importance of emission inventory,
499 scavenging assumptions, meteorological data and resolution for the modeled aerosol distributions
500 and model performance.

501

502 Global aerosol burdens and AOD in each sensitivity run are summarized in Table 3. The BC
503 burden is particularly sensitive to reduced scavenging by large-scale ice clouds (LSIDEC),
504 resulting in a 40% higher burden compared to the baseline. In contrast, an equal increase in the
505 scavenging efficiency (LSIINC) result in a decrease in burden of only 9%, while decreased
506 scavenging by liquid precipitation (SOLDEC) gives a 13% higher burden. The lower BC emissions
507 in the ECLv5 and CMIP5 inventories give a global BC burden that is 9 and 22% lower, respectively.
508 For sulfate, ammonium and OA, we also find the largest burden changes in the LSIDEC case,
509 followed by SOLDEC. The change in the LSIDEC is particularly large for OA and is driven by
510 changes in SOA. For SOA, the changes are determined not only by modifying the scavenging, but
511 also by changes in POA concentrations, which gas-phase secondary organics can partition onto.
512 Increasing the horizontal resolution results in a slightly higher burden for all species, except sea
513 salt.

514 While sensitivity tests may give similar changes in the total global burdens, the spatial distribution
515 of changes can differ substantially. Figure 4 shows the ratio of AOD and total burden by species
516 and altitude in each sensitivity simulation to the baseline. As expected, varying the emission
517 inventories results in changes that are largely confined to the main source regions (Figs.4a,b).
518 Using the CMIP5 inventory results in considerably lower concentrations over Asia, the Middle
519 East and North Africa, reflecting the higher emissions in the more recent inventory. Over Europe
520 and most of North America there is an increase, particularly for sulfate, nitrate and ammonium. A
521 similar pattern is found when using ECLv5, but the differences are smaller. Reducing the large-
522 scale ice cloud scavenging increases aerosol burdens the most at high latitudes, while changes in
523 the solubility assumption for liquid clouds affects burdens mostly over Asia, where emissions are
524 highest, and around the equator where convective activity is stronger. Changes in burdens when
525 using meteorological data from a different year are more heterogeneous and mainly occur in
526 regions where the influence of differences in the ENSO is expected to be the main factor, e.g.,
527 west coast of South America, South East Asia and Australia.



528 For BC, OA and dust, the largest impact relative to the baseline are seen above 600 hPa in the
529 LSIDEC case. Change in LSIDEC are also important in the case of sulfate and sea salt, but occur
530 at lower altitudes. In contrast to the other aerosol species, differences in emission inventories are
531 most important for nitrate. In a recent study, *Kipling et al.* [2016] investigated factors controlling
532 the vertical distribution of aerosols in the HadGEM3-UKCA. It was found that in-cloud
533 scavenging was very important in controlling the vertical mass concentration of all species, except
534 dust. For dust, it was also found that dry deposition and sub-cloud processes played key roles,
535 processes not examined in the present analysis. Moreover, *Kipling et al.* [2016] performed
536 sensitivity simulations by switching transport and scavenging on and off to get the full effect of a
537 given process, while we perform smaller perturbations to investigate uncertainties. Here we find
538 significant impacts of changes in ice-cloud removal efficiency on the vertical distribution of BC,
539 OA and dust, while large-scale liquid and convective precipitation is more important for sea salt
540 and nitrate

541 With the exception of different emission inventories, there is generally a small impact on surface
542 concentrations in source regions compared to the changes in remote areas. This is important to
543 note due to the role of aerosols in air quality perspectives, where uncertainties in near-source
544 concentrations are vital.

545 Our sensitivity tests show that changes in input data, resolution or scavenging can lead to notable
546 changes in the aerosol distributions. The next question is then how these changes affect model
547 performance compared to observations. Figure 5a compares modeled and measured surface
548 concentrations of BC, OC, sulfate and nitrate in each simulation using all observations in Fig. 1.
549 For BC, the sensitivity tests have little or no impact on correlation, but there is a markedly better
550 agreement in terms of standard deviation (i.e., model becomes closer to observations) for
551 CEDSv16/CMIP6 compared to RCP/CMIP5, reflecting the higher emissions in the former. Similar,
552 but smaller, effects are also found for the other species. The improvement from RCP/CMIP5 to
553 CEDSv16/CMIP6 is especially seen for measurements in Asia. A higher resolution is also found
554 to reduce the bias, in particular for BC. Figure 5b shows the comparison against AERONET AOD
555 in each sensitivity simulation. Again, there is a higher correlation and lower bias in the 1x1RES
556 run than in the baseline, while the opposite is found in the RCP/CMIP5 and ECLv5 cases. The
557 most pronounced changes results from using meteorological data from year 2000, in which case
558 the correlation is reduced from around 0.8 to 0.7.

559 For both observables, the difference in model performance between the baseline and scavenging
560 sensitivity tests is small. This may partly be an effect of the geographical coverage of stations; the
561 majority of measurements are from stations in more urban regions, whereas simulated burden
562 changes occur in remote regions, particularly at high latitudes and altitudes (Fig. 4). We therefore
563 also perform evaluations against AOD from regional sub-sets of AERONET stations. Ten of the
564 AERONET stations used in the present analysis are located north of 65°N (Fig. S1). A comparison
565 of monthly mean simulated AOD in each of the sensitivity runs against observations in this region
566 shows the best agreement with the baseline simulation and with the ECLv5 emission inventory,



567 with a considerably higher bias when scavenging parameters are modified (Fig. S7a). This is
568 particularly the case in the LSIDE run, where concentrations of all species increase at high
569 latitudes compared to the baseline (Fig. 4). In contrast, the reduced concentrations in LSIINC,
570 results in a negative bias. We note that most of these stations have missing values in the winter
571 months, which is when the model underestimate BC concentrations in the Arctic, hence limiting
572 the evaluation. Decreased scavenging efficiency also leads to a higher bias than in the baseline for
573 observations in Europe and North America (not shown). In Asia, where the model already
574 underestimates aerosols in the baseline configuration, the bias is reduced since concentrations
575 increase. However, differences are smaller than north of 65°N. Moreover, given the notable
576 exacerbation in model performance in other regions, it is likely that other sources of uncertainty
577 (e.g., emissions) are more important for the model-measurement discrepancies in Asia. A similar
578 comparison is performed for 15 AERONET stations located in North Africa and the Middle East
579 (Fig. S7b), where the dust influence is strong. Changing the meteorological year and reducing
580 scavenging results in higher dust burdens (Table 3). Again, the agreement is better in the baseline
581 run than in these sensitivity runs. In particular, the METDATA run result in a higher bias and a
582 lower correlation, which is not surprising as dust production depends also on meteorological
583 conditions. The changes compared to the baseline CEDSv16/CMIP6 simulation cannot be entirely
584 attributed to differences in dust concentrations, as seen from the RCP/CMIP5 and ECLv5
585 simulations where the dust production is equal to the baseline. Several studies have pointed to the
586 importance of spatial resolution for improved model performance compared to observations (e.g.,
587 [Sato *et al.*, 2016; Schutgens *et al.*, 2017; Schutgens *et al.*, 2016a; Wang *et al.*, 2016]). Wang *et al.*
588 [2016] found significant reductions in NMB of BC AAOD relative to AERONET when using a
589 high resolution (10 km) emission data and model output. In our analysis, moving from 2°x2° to
590 1°x1° horizontal resolution also results in a slightly higher correlation and reduced bias and errors
591 when compared to all AERONET stations (Fig. 5b). The impact is largest for AOD in China and
592 India, the NMB is reduced (from -34% and -24% (Fig. S6) to -20% and -10%, respectively).
593 However, the opposite effect is found for AERONET stations in Europe and North America. Of
594 course, the 1°x1° resolution is still very coarse compared to the grid sizes used in the
595 abovementioned studies.

596 Changes away from near-source areas are also evaluated in terms of BC concentrations by a
597 comparison with observed vertical distribution from the HIPPO3 campaign, where remote, marine
598 air over the Pacific was sampled across all latitudes (Sect. 2.5). To limit the number of model runs,
599 we focus on only one phase of the HIPPO campaign here, but a more comprehensive evaluation
600 of OsloCTM3 vertical BC distribution against aircraft measurements was performed by [Lund *et al.*,
601 2018]. Figure 6 shows observed average vertical BC concentration profiles against model
602 results from each sensitivity test. The OsloCTM3 reproduces the vertical distribution well in low
603 and mid-latitudes over the Pacific in its baseline configuration, although near-surface
604 concentrations in the tropics are underestimated. This is a significant improvement over the
605 OsloCTM2, where high-altitude concentrations in these regions typically were overestimated. The
606 baseline configuration of OsloCTM3 includes updates to the scavenging assumptions based on



607 previous studies investigating reasons for the high-altitude discrepancies (e.g., [Hodnebrog *et al.*,
608 2014; Lund *et al.*, 2017]. At high northern and southern latitudes, the model underestimates the
609 observed vertical profiles in the baseline. Increasing the model resolution does not have any
610 notable impact on the vertical profiles. There is a notable increase in high-latitude concentrations
611 when large-scale ice cloud scavenging is decreased. However, there is a simultaneous exacerbation
612 of model performance in the other latitude bands, pointing to potential tradeoffs when tuning
613 global parameters, as also illustrated by Lund *et al.* [2017]. Due to the significant altitude
614 dependence of the radiative effect of BC (e.g., [Samset *et al.*, 2013]), high altitude overestimations
615 will contribute significantly to uncertainties in BC RFari. We also note that HIPPO3 was
616 conducted in March/April: Comparison with aircraft measurements from other seasons show a
617 smaller underestimation at high latitudes ([Lund *et al.*, 2018].

618 3.3 Pre-industrial to present-day aerosols

619

620 With confidence in the model ability to reasonably represent current aerosol distributions
621 established, we next present an updated historical evolution of anthropogenic aerosols from pre-
622 industrial to present-day, and the consequent direct radiative effect (RFari). Figure 7 shows the net
623 change in total aerosol load from 1750 to 2014. Full times series by species are given in Table S4.
624 To keep in line with the terminology used in the IPCC AR5, we now separate out biomass burning
625 BC and POA in a separate species “biomass”. To illustrate the contributions from additional
626 emissions during the past 14 years, we also include the 2000-1750 difference. The values from the
627 present study are also compared with results from the AeroCom II models [Myhre *et al.*, 2013a],
628 where emissions over the period 1850 to 2000 from Lamarque *et al.* [2010] were used.

629 The most notable difference compared to the AeroCom II results is seen for biomass aerosols.
630 Biomass burning emissions have high interannual variability and this affects the analysis. While
631 the 1750-2014 difference is 0.23 mg m^{-2} , taking the difference between year 1750 and 2000 (black
632 asterisk) results in a net change of only 0.03 mg m^{-2} . There is also a much larger change in the
633 burden of biomass aerosols in the AeroCom experiments, reflecting a more than 100% higher
634 emissions in 2000 compared to 1850 Lamarque *et al.* [2010] inventory. However, biomass aerosols
635 comprises both scattering OA and absorbing BC and, as seen below, these nearly cancel in terms
636 of RFari. Changes in sulfate and OA from pre-industrial to 2000 are slightly higher in the present
637 analysis than in AeroCom II, and the influence of additional emissions since 2000 is seen. The
638 OsloCTM3fast is well below the AeroCom multi-model mean for nitrate. The OsloCTM2 was
639 found to be in the low range, but the multi-model was also influenced by some models giving high
640 estimates [Myhre *et al.*, 2013a]

641 Using the CEDSv16 emissions, we estimate a total net RFari from all anthropogenic aerosols in
642 2014 relative to 1750 of -0.17 W m^{-2} . The RFari from sulfate is -0.30 W m^{-2} , while the
643 contributions from OA (combined fossil fuel plus biofuel POA and SOA), nitrate and biomass
644 aerosols are smaller in magnitude of -0.09 , -0.02 and -0.0004 W m^{-2} , respectively. The RFari due
645 to fossil fuel and biofuel BC over the period is 0.31 W m^{-2} . The sum over the individual



646 contributions is non-linear with the total RFari, as found in previous studies (e.g., *Myhre et al.*
647 2013a).

648 Figure 8a shows the time series of RFari by component, as well as the total net, in the present
649 analysis (solid lines), and corresponding results reported in the IPCC AR5 (dashed lines). The net
650 RFari over time is mainly determined by the relative importance of compensating BC and sulfate
651 RFari. The most rapid increase in BC RFari is seen between 1950 and 1990, as emissions in Asia
652 started to grow, outweighing reductions in North America and Europe [*Hoesly et al.*, 2018]. After
653 a period of little change between 1990 and 2000, the rate of change increases again over the past
654 two decades, following strong emission increases in Asia and South Africa. Similarly, cooling
655 contribution from sulfate aerosols strengthened from around mid-century. However, in contrast to
656 BC, the evolution is fairly flat after 1990. The last 20 years has seen a continuous reduction in
657 sulfur dioxide (SO₂) emissions in Europe, from around 30 to 5 Tg yr⁻¹ in CEDSv16, with a similar
658 trend in North America. While emissions in China continue to increase well into the 2000s, a
659 stabilization is seen after 2010, following introduction of stricter emission limits as part of a
660 program to desulfurize power plants [*Klimont et al.*, 2013]. During the same period, emissions in
661 India have risen. However, the net global SO₂ emission trend over the past few years is a slight
662 decline [*Hoesly et al.*, 2018]. This development is reflected in the net RFari, which reaches its peak
663 (i.e., strongest negative value) around 1990 and gradually becomes weaker thereafter. This trend
664 is more pronounced in the present analysis than in the IPCC AR5 estimates, where the forcing due
665 to sulfate is more flat in recent decades, suggesting that projected emission estimates
666 underestimated recent decreases in SO₂. The minimum net RFari value is also reached later in the
667 latter. Moreover, a recent study suggests that current inventories underestimate the decline in
668 Chinese SO₂ emissions and estimate a 75% reduction since 2007 [*Li et al.*, 2017]. In this case, the
669 weakening trend could be even stronger than estimated here. The insert in Fig. 8a focuses on recent
670 estimates of total RFari over the period 1990-2015. Using the ECLv5 emission inventory, *Myhre*
671 *et al.* [2017] found a global mean RFari due to changes in aerosol abundances over the period
672 1990-2015 of 0.05 (±0.04) W m⁻². Our results using CEDSv16 emissions are in close agreement
673 with these findings.

674
675 The geographical shift in emissions is clearly reflected in zonally averaged RFari over time in Fig.
676 8b. RFari declined in magnitude north of 40°N after 1980, with particularly large year-to-year
677 decreases between 1990 and 1995, and from 2005 to 2010. The RFari has strengthened in
678 magnitude between 20°-30° in both hemispheres, although the peak around 35°N is considerably
679 weaker in 2014 than in 1980. The past decade, the net RFari has switched from negative to positive
680 north of 70°N, due to a combination of stronger positive RF of BC and from biomass burning
681 aerosols.

682
683 Here we have used an updated parameterization of BC absorption based on *Zanatta et al.* [2016]
684 (Sect. 2.4), which takes into account the ratio of non-BC-to-BC material and results in a MAC of



685 $12.5 \text{ m}^2 \text{ g}^{-1}$ at 550 nm. This is 26% higher than the $9.94 \text{ m}^2 \text{ g}^{-1}$ using the approach from *Bond and*
686 *Bergstrom* [2006]. Using the latter, we estimate a BC RFari in 2014 relative to 1750 of 0.23 W m^{-2} ,
687 25% lower than the 0.31 W m^{-2} calculated based on *Zanatta et al.* [2016]. These results
688 emphasize the importance of assumptions related to the BC absorption.

689 The magnitude of RFari by scattering aerosols is sensitive to assumptions about absorption by
690 organic aerosols, so-called brown carbon (BrC). Observational studies have provided evidence for
691 the existence of such particles, and modeling studies suggest they could be responsible for a
692 substantial fraction of total aerosol absorption, although the spread in estimates is wide (e.g., *Feng*
693 *et al.* [2013] and reference therein). In the present study we assume a considerable fraction of
694 absorption by OA (Sect. 2.4). Assuming purely scattering aerosols, the RFari from OA is -0.13 W
695 m^{-2} ; accounting for BrC absorption this is weakened to -0.09 W m^{-2} . Splitting total OA RFari into
696 contributions from primary and secondary aerosols, we find that purely scattering POA gives a
697 RFari of -0.07 W m^{-2} compared to -0.06 W m^{-2} with absorption. The corresponding numbers for
698 SOA are -0.06 and -0.03 W m^{-2} . This indicates that in OsloCTM3, the absorbing properties of SOA
699 are relatively more important than for POA. This is likely due to the generally higher altitude of
700 SOA than POA (Fig. S8) in combination with the increasing radiative efficiency of absorbing
701 aerosols with altitude [*Samset et al.*, 2013]. However, due to the weaker overall contributions from
702 OA, our results indicate that differences in parameterization of BC absorption can be more
703 important than uncertainties in absorption by BrC for the total net RFari.

704

705 4 Discussion

706

707 Our estimate of total net RFari in 2014 relative to 1750 is weaker in magnitude than the best
708 estimate for the 1750–2010 period reported by IPCC AR5. The difference is due to a combination
709 of factors, including weaker contributions from both cooling aerosols and BC. A significant range
710 from -0.6 to -0.13 W m^{-2} surrounds the central RFari estimate of -0.35 W m^{-2} from IPCC AR5
711 [*Boucher et al.*, 2013], due to the large spread in underlying simulated aerosol distributions. As
712 shown in Sect. 3, the OsloCTM3 generally lies close to or above the multi-model mean of
713 anthropogenic aerosol burdens from recent studies and performs reasonably well compared with
714 observations and other global models, with improvements over the predecessor OsloCTM2.

715 In particular, recent progress towards constraining the vertical distribution of BC concentrations
716 has resulted in improved agreement between modeled and observed vertical BC profiles over the
717 Pacific Ocean with less of the high-altitude overestimation seen in earlier studies. However, as
718 shown by *Lund et al.* [2018], discrepancies compared to recent aircraft measurements over the
719 Atlantic Ocean remain. The higher emissions in the CEDSV16 inventory also results in an
720 improved agreement with BC surface concentrations over Asia. Despite these considerably higher
721 emissions compared to older inventories, we calculate a weaker BC RFari than reported in AR5,
722 hence going in the opposite direction of explaining the difference to IPCC AR5 total RFari. The
723 IPCC AR5 best estimate for fossil fuel and biofuel BC of 0.4 (0.05 to 0.8) W m^{-2} [*Boucher et al.*,
724 2013] was based mainly on the two studies by *Myhre et al.* [2013a] and *Bond et al.* [2013], who



725 derived estimates of BC RFari of 0.23 (0.06 to 0.48) W m⁻² and 0.51 (0.06 to 0.91) W m⁻²,
726 respectively. The spread between the two is largely attributed to methodological differences: *Bond*
727 *et al.* [2013] used an observationally weighted scaling of results to match those based on
728 AERONET AAOD, which was not adopted by *Myhre et al.* [2013a]. Such ad-hoc adjustments
729 typically result in higher estimates (*Wang et al.* [2018] and references therein). Moreover, a recent
730 study by *Wang et al.* [2018] suggest that representativeness error arising when constraining coarse
731 resolution models with AERONET AAOD could result in a 30% overestimation of BC RFari,
732 which explains some of the differences between bottom-up and observationally constrained
733 numbers. The BC RFari estimate from the present study is around 20% higher than the AeroCom
734 multi-model mean from *Myhre et al.* [2013a] when calculated over the same period 1850-2000.
735 This reflects the higher emissions in the CEDSv16 emission inventory than in *Lamarque et al.*
736 [2010], as well as a higher MAC.

737 In general, we find lower surface sulfate concentrations in the model compared with measurements.
738 This could contribute to an underestimation of the sulfate RFari, which is weaker in the present
739 study than in IPCC AR5. We also note that the global mean sulfate burden is higher in the
740 OsloCTM3 than in most of the global models participating in the AeroCom III experiment (Sect.
741 3.1, *Bian et al.* [2017]). Compared with other AeroCom Phase III models, the OsloCTM3 performs
742 similarly or better in terms of nitrate and sulfate surface concentrations from CASTNET [*Bian et*
743 *al.*, 2017]. Nevertheless, the model diversity in simulated nitrate and sulfate remains large and,
744 although all models capture the main observed features in concentrations, further work is needed
745 to resolve the differences and improve model performance for these species.

746 While a comprehensive quantitative uncertainty analysis of the updated RFari estimate is not
747 possible within the scope of this study, we explore the order of magnitude uncertainties due to
748 “internal” factors such as scavenging parameterizations and model resolution by performing
749 sensitivity tests. Changes in global burden on the order of 10-20%, and up to 65%, were found
750 (Sect. 3.2). However, compared to observations of surface concentrations in near-source regions,
751 total AOD and vertical distribution of BC concentrations, we saw that the model generally
752 performed the best in its baseline configuration. Furthermore, the largest changes in the simulated
753 AOD and aerosol distributions were found in high-latitude regions, whereas changes over land
754 where the concentrations, and hence subsequent RF is localized, were smaller. For certain regions
755 and observables, there were notable differences between the baseline and sensitivity simulations.
756 For instance, an improvement in the baseline compared to using the CMIP5 emission inventory was
757 seen for BC surface concentrations, in particular in Asia, while the NMB of AOD compared to
758 AERONET stations in the same region was reduced in the simulation with higher spatial resolution.
759 The importance of using the correct meteorological year was also seen. Such uncertainties will
760 translate to the RFari estimates, along with uncertainties in optical properties such as absorption
761 by organic aerosols and parameterization of BC absorption (Sect. 3.3).

762

763 Estimates of radiative impacts depend critically on the confidence in the emission inventories. A
764 detailed discussion of uncertainties in the CEDS inventory is provided by *Hoesly et al.* [2018]. On
765 a global level, the uncertainty in SO₂ emissions tend to be relatively low, although there is an



766 indication of missing SO₂ sources in particular in the Persian Gulf [*McLinden et al.*, 2016], whereas
767 emission factors for BC, OC, NO_x, CO and VOCs have higher uncertainties. Uncertainties in
768 country-specific emissions can also be much larger, which is particularly true for carbonaceous
769 aerosols. In future CEDS versions, a quantitative uncertainty analysis is planned [*Hoesly et al.*,
770 2018], which will provide valuable input to modeling studies.

771

772 Our study does not include anthropogenic dust, i.e., wind-blown dust from soils disturbed by
773 human activities such as land use practices, deforestation and agriculture, and fugitive combustion
774 and industrial dust from urban sources. These sources could contribute an important fraction of
775 emissions and ambient PM_{2.5} concentrations in some regions [*Paul et al.*, 2012; *Sajeev et al.*, 2017],
776 but are missing from most models today. For instance, a recent study found a 2–16 mg m⁻³ increase
777 in PM_{2.5} concentrations in East and South Asia from anthropogenic fugitive, combustion, and
778 industrial dust emissions. However, the transport processes and optical properties, and hence,
779 radiative impact, is poorly known. We also do not include the effect of aerosol-cloud interactions,
780 which are crucial for the net climate impact of aerosols. For instance, recent studies suggest that
781 the impact of BC on global temperature response is small due to largely compensating direct and
782 semi-direct effects [*Samset and Myhre*, 2015; *Stjern et al.*, 2017]. The composition and distribution
783 of aerosols and oxidants in the pre-industrial atmosphere is uncertain and poorly constrained by
784 observations. However, while this is an important source of uncertainty in estimates of RF due to
785 aerosol-induced cloud albedo changes, it is less important for RFari because the forcing scales
786 quite linearly with aerosol burden [*Carlaw et al.*, 2017].

787

788

789 5 Conclusions

790

791 In this study, we have documented the third generation of the Oslo chemical transport model
792 (OsloCTM3) and evaluated the simulated distributions of aerosols, including results from a range
793 of simulations to investigate the sensitivity to uncertainties in scavenging processes, input of
794 emissions and meteorological data and resolution. We have then used the new historical CEDS
795 emission inventory (version 2016; CEDSv16), which will also be used in the upcoming CMIP6,
796 to simulate the temporal evolution of atmospheric concentrations of anthropogenic aerosols, and
797 quantified the temporal evolution of the subsequent radiative forcing due to aerosol-radiation
798 interactions (RFari).

799

800 The total AOD from the OsloCTM3 is in good agreement with observations from the AERONET
801 network with a correlation of 0.82 and a normalized mean bias (NMB) of -11.8%. Regionally, the
802 underestimation of observed AOD is higher for stations in China and India than in Europe and
803 North America, as also reflected from the comparison against measured aerosol surface
804 concentrations. High correlations 0.80-0.90 are also found for surface concentrations of BC, OC,
805 sulfate and nitrate aerosols compared with all measurements across Europe, North America and



806 Asia. The corresponding NMB range from -23% for BC and nitrate to -46% and -52% for OC and
807 sulfate, respectively. The OsloCTM3 performs notably better than its predecessor OsloCTM2 in
808 terms of high-altitude BC distribution as compared with observed BC concentration profiles over
809 the Pacific Ocean from the HIPPO3 campaign. In contrast, the model continues to underestimate
810 observed surface levels of BC during winter and spring. Compared with other recent estimates of
811 aerosol burdens, the OsloCTM3 generally lies close to or above the mean of other global models.

812 Increasing or reducing the scavenging efficiency, moving to a finer resolution, and using the wrong
813 meteorological year or a different emission inventory results in changes in the global mean aerosol
814 burdens of up to 65%. The burdens of BC, OC and sulfate are particularly sensitive to a reduced
815 efficiency of removal by large-scale ice clouds; a 10 percentage point reduction increases the
816 global burden by 40%, 65% and 20%, respectively. A corresponding increase in the efficiency
817 gives around 10% lower burdens. A significantly better agreement with BC surface concentrations
818 is found when using the CEDSv16 emission inventory compared with the RCP4.5. Furthermore,
819 a notable reduction in the bias of AOD compared to AERONET observations in Asia is found
820 when increasing the horizontal resolution, while the correlation is reduced when using the wrong
821 meteorological year. However, we find no clear evidence of consistently better model performance
822 across all observables and regions in the sensitivity tests than in the baseline configuration. This
823 may in part be influenced by the geographical coverage of observations, as the largest differences
824 in concentrations and AOD from the baseline is found at high altitudes and latitudes where the
825 availability of constraining measurements is limited.

826 Using the CEDSv16 historical emission inventory we estimate a total net R_{Fari} from all
827 anthropogenic aerosols, relative to 1750, of -0.17 W m^{-2} . This is significantly weaker than the best
828 estimate reported in the IPCC AR5, due to a combination of factors resulting in weaker
829 contributions from both cooling aerosols and BC in our simulations. Our updated R_{Fari} estimate
830 is based on a single global model. As shown by previous studies, there is a large spread estimates
831 of R_{Fari} due to the spread in modeled aerosol distributions. The present analysis shows that
832 uncertainties in emissions, scavenging and optical properties of aerosols can have important
833 impacts on the simulated AOD and subsequent forcing estimates within one model. Additional
834 studies to place our estimates in the context of multi-model spread and provide a comprehensive
835 uncertainty analysis are needed ahead of the IPCC Sixth Assessment Report.

836

837

838 Data availability

839 The CEDS anthropogenic emissions data is published within the ESGF system [https://esgf-](https://esgf-node.llnl.gov/search/input4mips/)
840 [node.llnl.gov/search/input4mips/](https://esgf-node.llnl.gov/search/input4mips/). Surface observations used in this study are collected from the
841 following publicly available databases: the EBAS database (<http://ebas.nilu.no/>) hosted by NILU
842 – Norwegian Institute for Air Research. The US national Clean Air Status and Trends monitoring
843 network (CASTNET), available at <http://www.epa.gov/castnet>. The Interagency Monitoring of



844 Protected Visual Environments (IMPROVE), a collaborative association of state, tribal, and
845 federal agencies, and international partners, with the US EPA as the primary funding source and
846 support from the National Park Service. Data available from
847 <http://vista.cira.colostate.edu/Improve/>. MODIS and MISR AOD retrievals are downloaded from
848 <https://giovanni.gsfc.nasa.gov/giovanni/>. Aircraft measurements from the HIPPO3 flights
849 available from <https://www.eol.ucar.edu/node/524>. Model output available upon request from
850 Marianne T. Lund (m.t.lund@cicero.oslo.no).

851
852

853 Acknowledgements

854 MTL, GUM, AHS, RBS acknowledges funding from the Norwegian Research Council through
855 grants 250573 (SUPER) and 24883 (QUISARC). The National Center for Atmospheric Research
856 (NCAR) is sponsored by the National Science Foundation (NSF). We would like to express our
857 thanks to all those who are involved in AERONET, IMPROVE, CASTNET, EMEP and ACTRIS
858 measurements efforts and have contributed through operating sites, performing chemical analysis
859 and by submissions of data to public data bases. The authors also acknowledge funding of the
860 Horizon 2020 research and innovation programme ACTRIS-2 Integrating Activities (IA) (grant
861 agreement No 654109). We also acknowledge the Research Council of Norway's programme for
862 supercomputing (NOTUR). The AeroCom database is maintained through basic funding from the
863 Norwegian Meteorological Institute.

864
865
866

867 Competing interests

868 The authors declare that they have no conflict of interest.

869
870
871
872

873 References

874
875
876
877

Amann, M., et al. (2011), Cost-effective control of air quality and greenhouse gases in Europe:
Modeling and policy applications, *Environmental Modelling & Software*, 26(12), 1489-1501,
[doi:http://dx.doi.org/10.1016/j.envsoft.2011.07.012](http://dx.doi.org/10.1016/j.envsoft.2011.07.012).

878
879
880
881

Berglen, T. F., T. K. Berntsen, I. S. A. Isaksen, and J. K. Sundet (2004), A global model of the
coupled sulfur/oxidant chemistry in the troposphere: The sulfur cycle, *Journal of Geophysical Research-
Atmospheres*, 109(D19), doi:10.1029/2003jd003948.

882



- 883 Berntsen, T., J. Fuglestedt, G. Myhre, F. Stordal, and T. F. Berglen (2006), Abatement of
884 greenhouse gases: Does location matter?, *Climatic Change*, 74(4), 377-411, doi:10.1007/s10584-006-
885 0433-4.
- 886
887 Bian, H., et al. (2017), Investigation of global nitrate from the AeroCom Phase III experiment,
888 *Atmos. Chem. Phys. Discuss.*, 2017, 1-44, doi:10.5194/acp-2017-359.
- 889
890 Bond, T. C., and R. W. Bergstrom (2006), Light absorption by carbonaceous particles: An
891 investigative review, *Aerosol Science and Technology*, 40(1), 27-67, doi:10.1080/02786820500421521.
- 892
893 Bond, T. C., et al. (2013), Bounding the role of black carbon in the climate system: A scientific
894 assessment, *Journal of Geophysical Research: Atmospheres*, 118(11), 5380-5552,
895 doi:10.1002/jgrd.50171.
- 896
897 Boucher, O., et al. (2013), Clouds and Aerosols: In: Climate Change 2013: The Physical Science
898 Basis. Contribution of Working Group I to the Fifth Assessment Report of the Intergovernmental Panel
899 on Climate Change [Stocker, T.F., D. Qin, G.-K. Plattner, M. Tignor, S.K. Allen, J. Boschung, A. Nauels, Y.
900 Xia, V. Bex and P.M. Midgley (eds.)]. Cambridge University Press, Cambridge, United Kingdom and New
901 York, NY, USA.
- 902
903 Bourgeois, Q., and I. Bey (2011), Pollution transport efficiency toward the Arctic: Sensitivity to
904 aerosol scavenging and source regions, *Journal of Geophysical Research: Atmospheres*, 116(D8), n/a-n/a,
905 doi:10.1029/2010JD015096.
- 906
907 Browse, J., K. S. Carslaw, S. R. Arnold, K. Pringle, and O. Boucher (2012), The scavenging
908 processes controlling the seasonal cycle in Arctic sulphate and black carbon aerosol, *Atmospheric
909 Chemistry and Physics*, 12(15), 6775-6798, doi:10.5194/acp-12-6775-2012.
- 910
911 Carslaw, K. S., H. Gordon, D. S. Hamilton, J. S. Johnson, L. A. Regayre, M. Yoshioka, and K. J.
912 Pringle (2017), Aerosols in the Pre-industrial Atmosphere, *Current Climate Change Reports*, 3(1), 1-15,
913 doi:10.1007/s40641-017-0061-2.
- 914
915 Cavalli, F., et al. (2016), A European aerosol phenomenology -4: Harmonized concentrations of
916 carbonaceous aerosol at 10 regional background sites across Europe, *Atmospheric Environment*, 144,
917 133-145, doi:<https://doi.org/10.1016/j.atmosenv.2016.07.050>.
- 918
919 Dubovik, O., and M. D. King (2000), A flexible inversion algorithm for retrieval of aerosol optical
920 properties from Sun and sky radiance measurements, *Journal of Geophysical Research: Atmospheres*,
921 105(D16), 20673-20696, doi:10.1029/2000JD900282.
- 922



- 923 Eckhardt, S., et al. (2015), Current model capabilities for simulating black carbon and sulfate
924 concentrations in the Arctic atmosphere: a multi-model evaluation using a comprehensive measurement
925 data set, *Atmos. Chem. Phys.*, *15*(16), 9413-9433, doi:10.5194/acp-15-9413-2015.
- 926
927 Fan, S. M., J. P. Schwarz, J. Liu, D. W. Fahey, P. Ginoux, L. W. Horowitz, H. Levy, Y. Ming, and J. R.
928 Spackman (2012), Inferring ice formation processes from global-scale black carbon profiles observed in
929 the remote atmosphere and model simulations, *Journal of Geophysical Research: Atmospheres*,
930 *117*(D23), n/a-n/a, doi:10.1029/2012JD018126.
- 931
932 Feng, Y., V. Ramanathan, and V. R. Kotamarthi (2013), Brown carbon: a significant atmospheric
933 absorber of solar radiation?, *Atmos. Chem. Phys.*, *13*(17), 8607-8621, doi:10.5194/acp-13-8607-2013.
- 934
935 Gantt, B., M. S. Johnson, M. Crippa, A. S. H. Prévôt, and N. Meskhidze (2015), Implementing
936 marine organic aerosols into the GEOS-Chem model, *Geosci. Model Dev.*, *8*(3), 619-629,
937 doi:10.5194/gmd-8-619-2015.
- 938
939 Granier, C., et al. (2011), Evolution of anthropogenic and biomass burning emissions of air
940 pollutants at global and regional scales during the 1980–2010 period, *Climatic Change*, *109*(1), 163,
941 doi:10.1007/s10584-011-0154-1.
- 942
943 Grini, A., G. Myhre, J. K. Sundet, and I. S. A. Isaksen (2002), Modeling the annual cycle of sea salt
944 in the global 3D model Oslo CTM2: Concentrations, fluxes, and radiative impact, *Journal of Climate*,
945 *15*(13), 1717-1730, doi:10.1175/1520-0442(2002)015<1717:mtacos>2.0.co;2.
- 946
947 Grini, A., G. Myhre, C. S. Zender, and I. S. A. Isaksen (2005), Model simulations of dust sources
948 and transport in the global atmosphere: Effects of soil erodibility and wind speed variability, *Journal of*
949 *Geophysical Research-Atmospheres*, *110*(D2), doi:10.1029/2004jd005037.
- 950
951 Hodnebrog, Ø., G. Myhre, and B. H. Samset (2014), How shorter black carbon lifetime alters its
952 climate effect, *Nat Commun*, *5*, doi:10.1038/ncomms6065.
- 953
954 Hoesly, R. M., et al. (2018), Historical (1750–2014) anthropogenic emissions of reactive gases
955 and aerosols from the Community Emission Data System (CEDS), *Geosci. Model Dev.*, *2018*(11), 369-408,
956 doi:<https://doi.org/10.5194/gmd-11-369-2018>.
- 957
958 Holben, B. N., et al. (1998), AERONET—A Federated Instrument Network and Data Archive for
959 Aerosol Characterization, *Remote Sensing of Environment*, *66*(1), 1-16,
960 doi:[https://doi.org/10.1016/S0034-4257\(98\)00031-5](https://doi.org/10.1016/S0034-4257(98)00031-5).
- 961
962 Hoyle, C. R., T. Berntsen, G. Myhre, and I. S. A. Isaksen (2007), Secondary organic aerosol in the
963 global aerosol-chemical transport model Oslo CTM2, *Atmos. Chem. Phys.*, *7*(5675-5694).



- 964
965 Jaeglé, L., P. K. Quinn, T. S. Bates, B. Alexander, and J. T. Lin (2011), Global distribution of sea salt
966 aerosols: new constraints from in situ and remote sensing observations, *Atmos. Chem. Phys.*, *11*(7),
967 3137-3157, doi:10.5194/acp-11-3137-2011.
- 968
969 Kinne, S., D. O'Donnell, P. Stier, S. Kloster, K. Zhang, H. Schmidt, S. Rast, M. Giorgetta, T. F. Eck,
970 and B. Stevens (2013), MAC-v1: A new global aerosol climatology for climate studies, *J. Adv. Model.*
971 *Earth Syst.*, *5*, 704-740, doi:doi:10.1002/jame.20035.
- 972
973 Kipling, Z., et al. (2016), What controls the vertical distribution of aerosol? Relationships
974 between process sensitivity in HadGEM3–UKCA and inter-model variation from AeroCom Phase II,
975 *Atmos. Chem. Phys.*, *16*(4), 2221-2241, doi:10.5194/acp-16-2221-2016.
- 976
977 Kipling, Z., P. Stier, J. P. Schwarz, A. E. Perring, J. R. Spackman, G. W. Mann, C. E. Johnson, and P.
978 J. Telford (2013), Constraints on aerosol processes in climate models from vertically-resolved aircraft
979 observations of black carbon, *Atmos. Chem. Phys.*, *13*(12), 5969-5986, doi:10.5194/acp-13-5969-2013.
- 980
981 Kirchstetter, T. W., T. Novakov, and P. V. Hobbs (2004), Evidence that the spectral dependence
982 of light absorption by aerosols is affected by organic carbon, *Journal of Geophysical Research:*
983 *Atmospheres*, *109*(D21), n/a-n/a, doi:10.1029/2004JD004999.
- 984
985 Klimont, Z., K. Kupiainen, C. Heyes, P. Purohit, J. Cofala, P. Rafaj, J. Borcken-Kleefeld, and W.
986 Schöpp (2017), Global anthropogenic emissions of particulate matter including black carbon, *Atmos.*
987 *Chem. Phys.*, *17*(14), 8681-8723, doi:10.5194/acp-17-8681-2017.
- 988
989 Klimont, Z., S. J. Smith, and J. Cofala (2013), The last decade of global anthropogenic sulfur
990 dioxide: 2000–2011 emissions, *Environmental Research Letters*, *8*(1), 014003.
- 991
992 Kumar, R., M. C. Barth, G. G. Pfister, V. S. Nair, S. D. Ghude, and N. Ojha (2015), What controls
993 the seasonal cycle of black carbon aerosols in India?, *Journal of Geophysical Research: Atmospheres*,
994 *120*(15), 7788-7812, doi:10.1002/2015JD023298.
- 995
996 Lamarque, J. F., et al. (2010), Historical (1850–2000) gridded anthropogenic and biomass
997 burning emissions of reactive gases and aerosols: methodology and application, *Atmos. Chem. Phys.*,
998 *10*(15), 7017-7039, doi:10.5194/acp-10-7017-2010.
- 999
1000 Lavery, T. F., C. M. Rogers, R. Baumgardner, and K. P. Mishoe (2009), Intercomparison of Clean
1001 Air Status and Trends Network Nitrate and Nitric Acid Measurements with Data from Other Monitoring
1002 Programs, *Journal of the Air & Waste Management Association*, *59*(2), 214-226, doi:10.3155/1047-
1003 3289.59.2.214.
- 1004



- 1005 Lee, Y. H., et al. (2013), Evaluation of preindustrial to present-day black carbon and its albedo
1006 forcing from Atmospheric Chemistry and Climate Model Intercomparison Project (ACCMIP), *Atmospheric*
1007 *Chemistry and Physics*, 13(5), 2607-2634, doi:10.5194/acp-13-2607-2013.
- 1008
1009 Li, C., et al. (2017), India Is Overtaking China as the World's Largest Emitter of Anthropogenic
1010 Sulfur Dioxide, *Scientific Reports*, 7(1), 14304, doi:10.1038/s41598-017-14639-8.
- 1011
1012 Lund, M. T., and T. Berntsen (2012), Parameterization of black carbon aging in the OsloCTM2
1013 and implications for regional transport to the Arctic, *Atmos. Chem. Phys.*, 12(15), 6999-7014,
1014 doi:10.5194/acp-12-6999-2012.
- 1015
1016 Lund, M. T., T. K. Berntsen, and B. H. Samset (2017), Sensitivity of black carbon concentrations
1017 and climate impact to aging and scavenging in OsloCTM2-M7, *Atmos. Chem. Phys.*, 17(9), 6003-6022,
1018 doi:10.5194/acp-17-6003-2017.
- 1019
1020 Lund, M. T., B. H. Samset, R. B. Skeie, D. Watson-Parris, J. M. Katich, J. P. Schwarz, and B.
1021 Weinzierl (2018), Short Black Carbon lifetime inferred from a global set of aircraft observations, in
1022 review.
- 1023
1024 Mahmood, R., K. von Salzen, M. Flanner, M. Sand, J. Langner, H. Wang, and L. Huang (2016),
1025 Seasonality of global and Arctic black carbon processes in the Arctic Monitoring and Assessment
1026 Programme models, *Journal of Geophysical Research: Atmospheres*, 121(12), 7100-7116,
1027 doi:10.1002/2016JD024849.
- 1028
1029 McLinden, C. A., V. Fioletov, M. W. Shephard, N. Krotkov, C. Li, R. V. Martin, M. D. Moran, and J.
1030 Joiner (2016), Space-based detection of missing sulfur dioxide sources of global air pollution, *Nature*
1031 *Geoscience*, 9, 496, doi:10.1038/ngeo2724
- 1032 <https://www.nature.com/articles/ngeo2724#supplementary-information>.
- 1033
1034 Metzger, S., F. Dentener, M. Krol, A. Jeuken, and J. Lelieveld (2002a), Gas/aerosol partitioning -
1035 2. Global modeling results, *Journal of Geophysical Research-Atmospheres*, 107(D16),
1036 doi:10.1029/2001jd001103.
- 1037
1038 Metzger, S., F. Dentener, S. Pandis, and J. Lelieveld (2002b), Gas/aerosol partitioning: 1. A
1039 computationally efficient model, *Journal of Geophysical Research-Atmospheres*, 107(D16),
1040 doi:10.1029/2001jd001102.
- 1041
1042 MISR (2018), Data product specification for the MISR level 2 aerosol product, Garay, M.J., et al.,
1043 https://eosweb.larc.nasa.gov/project/misr/DPS_AEROSOL_V023.20180125.pdf (accessed 04/26/2018),
1044 edited.
- 1045



- 1046 MOD08 (2018), MODIS Level 3 Atmosphere Products (MOD 08), Data Products Handbook
1047 Volume 2. https://modis.gsfc.nasa.gov/data/dataproduct/dataproducts.php?MOD_NUMBER=08 (accessed
1048 04/26/2018).
- 1049
1050 Myhre, G., et al. (2017), Multi-model simulations of aerosol and ozone radiative forcing due to
1051 anthropogenic emission changes during the period 1990–2015, *Atmos. Chem. Phys.*, 17(4), 2709-2720,
1052 doi:10.5194/acp-17-2709-2017.
- 1053
1054 Myhre, G., et al. (2007), Comparison of the radiative properties and direct radiative effect of
1055 aerosols from a global aerosol model and remote sensing data over ocean, *Tellus B*, 59(1), 115-129,
1056 doi:10.1111/j.1600-0889.2006.00226.x.
- 1057
1058 Myhre, G., et al. (2009), Modelled radiative forcing of the direct aerosol effect with multi-
1059 observation evaluation, *Atmospheric Chemistry and Physics*, 9(4), 1365-1392, doi:10.5194/acp-9-1365-
1060 2009.
- 1061
1062 Myhre, G., A. Grini, and S. Metzger (2006), Modelling of nitrate and ammonium-containing
1063 aerosols in presence of sea salt, *Atmos. Chem. Phys.*, 6, 4809-4821.
- 1064
1065 Myhre, G., et al. (2013a), Radiative forcing of the direct aerosol effect from AeroCom Phase II
1066 simulations, *Atmos. Chem. Phys.*, 13(4), 1853-1877, doi:10.5194/acp-13-1853-2013.
- 1067
1068 Myhre, G., et al. (2013b), Anthropogenic and natural radiative forcing. In: Climate Change 2013:
1069 The Physical Science Basis. Contribution of Working Group I to the Fifth Assessment Report of the
1070 Intergovernmental Panel on Climate Change [Stocker, T.F., D., Qin, G.-K. Plattner, M. Tignor, S.K. Allen, J.
1071 Boschung, A. Nauels, Y. Xia, V. Bex and P.M. Midgley (eds). Cambridge University Press, Cambridge,
1072 United Kingdom and New York, NY, USA
- 1073
1074 Paul, G., P. J. M., G. T. E., H. N. Christina, and Z. Ming (2012), Global - scale attribution of
1075 anthropogenic and natural dust sources and their emission rates based on MODIS Deep Blue aerosol
1076 products, *Reviews of Geophysics*, 50(3), doi:doi:10.1029/2012RG000388.
- 1077
1078 Petzold, A., et al. (2013), Recommendations for reporting "black carbon" measurements, *Atmos.*
1079 *Chem. Phys.*, 13(16), 8365-8379, doi:10.5194/acp-13-8365-2013.
- 1080
1081 Putaud, J. P., et al. (2010), A European aerosol phenomenology – 3: Physical and chemical
1082 characteristics of particulate matter from 60 rural, urban, and kerbside sites across Europe, *Atmospheric*
1083 *Environment*, 44(10), 1308-1320, doi:<https://doi.org/10.1016/j.atmosenv.2009.12.011>.
- 1084
1085 Randerson, J. T., G. R. van der Werf, L. Giglio, G. J. Collatz, and P. S. Kasibhatla (2017), Global Fire
1086 Emissions Database, Version 4.1 (GFEDv4). ORNL DAAC, Oak Ridge, Tennessee, USA. ,
1087 doi:<https://doi.org/10.3334/ORNLDAAAC/1293>.



- 1088
1089 Sajeev, P., et al. (2017), Anthropogenic fugitive, combustion and industrial dust is a significant,
1090 underrepresented fine particulate matter source in global atmospheric models, *Environmental Research*
1091 *Letters*, 12(4), 044018.
- 1092
1093 Samset, B. H., and G. Myhre (2015), Climate response to externally mixed black carbon as a
1094 function of altitude, *Journal of Geophysical Research: Atmospheres*, 120(7), 2913-2927,
1095 doi:10.1002/2014JD022849.
- 1096
1097 Samset, B. H., et al. (2014), Modelled black carbon radiative forcing and atmospheric lifetime in
1098 AeroCom Phase II constrained by aircraft observations, *Atmos. Chem. Phys.*, 14(22), 12465-12477,
1099 doi:10.5194/acp-14-12465-2014.
- 1100
1101 Samset, B. H., et al. (2013), Black carbon vertical profiles strongly affect its radiative forcing
1102 uncertainty, *Atmos. Chem. Phys.*, 13(5), 2423-2434, doi:10.5194/acp-13-2423-2013.
- 1103
1104 Samset, B. H., C. W. Stjern, E. Andrews, R. A. Kahn, G. Myhre, M. Schulz, and G. L. Schuster
1105 (2018), Aerosol Absorption: Progress Towards Global and Regional Constraints, *Current Climate Change*
1106 *Reports*, doi:10.1007/s40641-018-0091-4.
- 1107
1108 Sato, Y., H. Miura, H. Yashiro, D. Goto, T. Takemura, H. Tomita, and T. Nakajima (2016),
1109 Unrealistically pristine air in the Arctic produced by current global scale models, *Scientific Reports*, 6,
1110 26561, doi:10.1038/srep26561
- 1111 <http://www.nature.com/articles/srep26561#supplementary-information>.
- 1112
1113 Schutgens, N., S. Tsyro, E. Gryspeerd, D. Goto, N. Weigum, M. Schulz, and P. Stier (2017), On
1114 the spatio-temporal representativeness of observations, *Atmos. Chem. Phys.*, 17(16), 9761-9780,
1115 doi:10.5194/acp-17-9761-2017.
- 1116
1117 Schutgens, N. A. J., E. Gryspeerd, N. Weigum, S. Tsyro, D. Goto, M. Schulz, and P. Stier (2016a),
1118 Will a perfect model agree with perfect observations? The impact of spatial sampling, *Atmos. Chem.*
1119 *Phys.*, 16(10), 6335-6353, doi:10.5194/acp-16-6335-2016.
- 1120
1121 Schutgens, N. A. J., D. G. Partridge, and P. Stier (2016b), The importance of temporal collocation
1122 for the evaluation of aerosol models with observations, *Atmos. Chem. Phys.*, 16(2), 1065-1079,
1123 doi:10.5194/acp-16-1065-2016.
- 1124
1125 Schwarz, J. P., B. H. Samset, A. E. Perring, J. R. Spackman, R. S. Gao, P. Stier, M. Schulz, F. L.
1126 Moore, E. A. Ray, and D. W. Fahey (2013), Global-scale seasonally resolved black carbon vertical profiles
1127 over the Pacific, *Geophysical Research Letters*, 40(20), 2013GL057775, doi:10.1002/2013GL057775.
- 1128



- 1129 Sindelarova, K., C. Granier, I. Bouarar, A. Guenther, S. Tilmes, T. Stavrou, J. F. Müller, U. Kuhn,
1130 P. Stefani, and W. Knorr (2014), Global data set of biogenic VOC emissions calculated by the MEGAN
1131 model over the last 30 years, *Atmos. Chem. Phys.*, *14*(17), 9317-9341, doi:10.5194/acp-14-9317-2014.
- 1132
1133 Skeie, R. B., T. Berntsen, G. Myhre, C. A. Pedersen, J. Ström, S. Gerland, and J. A. Ogren (2011),
1134 Black carbon in the atmosphere and snow, from pre-industrial times until present, *Atmospheric
1135 Chemistry and Physics*, *11*(14), 6809-6836, doi:10.5194/acp-11-6809-2011.
- 1136
1137 Smith, S. J., Y. Zhou, P. Kyle, H. Wang, and H. Yu (2015), A Community Emissions Data System
1138 (CEDS): Emissions for CMIP6 and Beyond. .
- 1139
1140 Sofiev, M., J. Soares, M. Prank, G. de Leeuw, and J. Kukkonen (2011), A regional-to-global model
1141 of emission and transport of sea salt particles in the atmosphere, *Journal of Geophysical Research:
1142 Atmospheres*, *116*(D21), n/a-n/a, doi:10.1029/2010JD014713.
- 1143
1144 Stamnes, K., S. C. Tsay, W. Wiscombe, and K. Jayaweera (1988), Numerically stable algorithm for
1145 discrete-ordinate-method radiative transfer in multiple scattering and emitting layered media, *Appl.
1146 Opt.*, *27*(12), 2502-2509, doi:10.1364/AO.27.002502.
- 1147
1148 Stjern, C. W., et al. (2017), Rapid Adjustments Cause Weak Surface Temperature Response to
1149 Increased Black Carbon Concentrations, *Journal of Geophysical Research: Atmospheres*, *122*(21), 11,462-
1150 411,481, doi:10.1002/2017JD027326.
- 1151
1152 Søvde, O. A., M. J. Prather, I. S. A. Isaksen, T. K. Berntsen, F. Stordal, X. Zhu, C. D. Holmes, and J.
1153 Hsu (2012), The chemical transport model Oslo CTM3, *Geosci. Model Dev.*, *5*(6), 1441-1469,
1154 doi:10.5194/gmd-5-1441-2012.
- 1155
1156 Thomson, A. M., et al. (2011), RCP4.5: a pathway for stabilization of radiative forcing by 2100,
1157 *Climatic Change*, *109*(1), 77, doi:10.1007/s10584-011-0151-4.
- 1158
1159 Tsigaridis, K., et al. (2014), The AeroCom evaluation and intercomparison of organic aerosol in
1160 global models, *Atmos. Chem. Phys.*, *14*(19), 10845-10895, doi:10.5194/acp-14-10845-2014.
- 1161
1162 Tørseth, K., W. Aas, K. Breivik, A. M. Fjæraa, M. Fiebig, A. G. Hjellbrekke, C. Lund Myhre, S.
1163 Solberg, and K. E. Yttri (2012), Introduction to the European Monitoring and Evaluation Programme
1164 (EMEP) and observed atmospheric composition change during 1972–2009, *Atmos. Chem. Phys.*,
1165 *12*(12), 5447-5481, doi:10.5194/acp-12-5447-2012.
- 1166
1167 van Marle, M. J. E., et al. (2017), Historic global biomass burning emissions for CMIP6 (BB4CMIP)
1168 based on merging satellite observations with proxies and fire models (1750–2015), *Geosci. Model Dev.*,
1169 *10*(9), 3329-3357, doi:10.5194/gmd-10-3329-2017.



- 1170
1171 van Vuuren, D. P., et al. (2011), The representative concentration pathways: an overview,
1172 *Climatic Change*, 109(1), 5, doi:10.1007/s10584-011-0148-z.
- 1173
1174 Wang, R., E. Andrews, Y. Balkanski, O. Boucher, G. Myhre, B. H. Samset, M. Schulz, G. L.
1175 Schuster, M. Valari, and S. Tao (2018), Spatial Representativeness Error in the Ground-Level Observation
1176 Networks for Black Carbon Radiation Absorption, *Geophysical Research Letters*, n/a-n/a,
1177 doi:10.1002/2017GL076817.
- 1178
1179 Wang, R., et al. (2016), Estimation of global black carbon direct radiative forcing and its
1180 uncertainty constrained by observations, *Journal of Geophysical Research: Atmospheres*, 121(10), 5948-
1181 5971, doi:10.1002/2015JD024326.
- 1182
1183 Wang, R., et al. (2014), Exposure to ambient black carbon derived from a unique inventory and
1184 high-resolution model, *Proceedings of the National Academy of Sciences*, 111(7), 2459-2463,
1185 doi:10.1073/pnas.1318763111.
- 1186
1187 Witek, M. L., D. J. Diner, and M. J. Garay (2016), Satellite assessment of sea spray aerosol
1188 productivity: Southern Ocean case study, *Journal of Geophysical Research: Atmospheres*, 121(2), 872-
1189 894, doi:10.1002/2015JD023726.
- 1190
1191 Wofsy, S. C., H. S. Team, T. Cooperating Modellers, and T. Satellite (2011), HIAPER Pole-to-Pole
1192 Observations (HIPPO): fine-grained, global-scale measurements of climatically important atmospheric
1193 gases and aerosols, *Philosophical Transactions of the Royal Society a-Mathematical Physical and*
1194 *Engineering Sciences*, 369(1943), 2073-2086, doi:10.1098/rsta.2010.0313.
- 1195
1196 Zanatta, M., et al. (2016), A European aerosol phenomenology-5: Climatology of black carbon
1197 optical properties at 9 regional background sites across Europe, *Atmospheric Environment*, 145, 346-
1198 364, doi:<https://doi.org/10.1016/j.atmosenv.2016.09.035>.
- 1199
1200 Zhang, X. Y., Y. Q. Wang, T. Niu, X. C. Zhang, S. L. Gong, Y. M. Zhang, and J. Y. Sun (2012),
1201 Atmospheric aerosol compositions in China: spatial/temporal variability, chemical signature, regional
1202 haze distribution and comparison with global models. , *Atmos. Chem. Phys.*, 12, 779-799.
- 1203
1204
1205
1206
1207
1208
1209
1210



1211 Tables

1212

1213 *Table 1: Summary and description of simulations in this study*

Name	Anthropogenic emissions	Year	Res	Description
CEDSv16/CMIP6	CEDS, version released in 2016	2010	2x2	Baseline simulation, 2.25x2.25 degree resolution
ECLv5	ECLIPSEv5	2010	2x2	As baseline, but with ECLIPSEv5 emissions
RCP/CMIP5	RCP4.5	2010	2x2	As baseline, but RCP4.5/CMIP5 emissions
LSIDEC	CEDS	2010	2x2	Reduced scavenging of all aerosols by large-scale ice clouds
LSIINC	CEDS	2010	2x2	Increased scavenging of all aerosols by large-scale ice clouds
SOLDEC	CEDS	2010	2x2	Decreased scavenging of all aerosols by convective and large-scale liquid precipitation
1x1RES	CEDS	2010	1x1	Same as baseline, but on 1.125x1.125 degree resolution
METDTA	CEDS	2010	2x2	Year 2010 emissions, but 2000 meteorology
Historical	CEDS/	1750-2014	2x2	Time-slice simulations for year 1750, 1850, 1900, 1910, 1920, 1930, 1940, 1950, 1960, 1970, 1980, 1985, 1990, 1995, 2000, 2005, 2010, 2014

1214

1215

1216

1217

1218

1219 *Table 2: Fraction of aerosol mass available for wet scavenging by convective, large-scale liquid*
 1220 *and large-scale ice precipitation in baseline setup and in the three sensitivity tests.*

1221 *Phil=hydrophilic, phob=hydrophobic.*

1222

Simulation	Precipitation type	Sulfate	OM phil	OM phob	BC phil	BC Phob	Nitrate	SOA	Sea salt	Dust
CEDSv16/CMIP6	Convective	1	1	1	1	1	1	0.8	1	1
	LS-liquid	1	1	0	1	0	1	0.8	1	1
	LS-ice	0.1	0.1	0.2	0.1	0.2	0.1	0.16	0.1	0.5
LSIINC	LS-ice	0.3	0.3	0.4	0.3	0.4	0.3	0.32	0.3	0.7
LSIDEC	LS-ice	0.001	0.001	0.1	0.001	0.1	0.001	0.001	0.001	0.1
SOLDEC	Convective	0.8	0.8	0.8	0.8	0.8	0.8	0.6	0.8	0.8
	LS-liquid	0.8	0.8	0	0.8	0	0.8	0.6	0.8	0.8

1223

1224

1225

1226

1227

1228

1229



1230

1231

1232 *Table 3: Global, annual mean aerosol burdens [mg m⁻²] and total AOD in the baseline and*
 1233 *sensitivity simulations*

Simulation	BC	OA	Sulfate	NH4 (fine+coarse)	Nitrate (fine)	Nitrate (coarse)	Sea salt	Dust	AOD
CEDSv16/CMIP6	0.23	3.4	5.4	0.68	0.17	3.9	12	39	0.13
ECLv5	0.21	3.1	5.1	0.65	0.15	3.7	12	39	0.13
RCP/CMIP5	0.18	3.2	5.3	0.63	0.13	3.7	12	39	0.13
LSIINC	0.21	2.8	4.9	0.63	0.17	3.4	11	39	0.12
LSIDEC	0.32	5.3	6.5	0.79	0.16	4.7	14	43	0.16
SOLDEC	0.26	3.6	6.1	0.78	0.16	5.2	15	42	0.15
1x1RES	0.24	3.4	5.6	0.71	0.19	3.6	12	38	0.14
METDTA	0.22	3.0	5.5	0.69	0.16	3.8	12	42	0.13

1234

1235

1236

1237

1238

1239

1240

1241

1242

1243

1244

1245

1246

1247

1248

1249

1250

1251

1252

1253

1254

1255

1256

1257

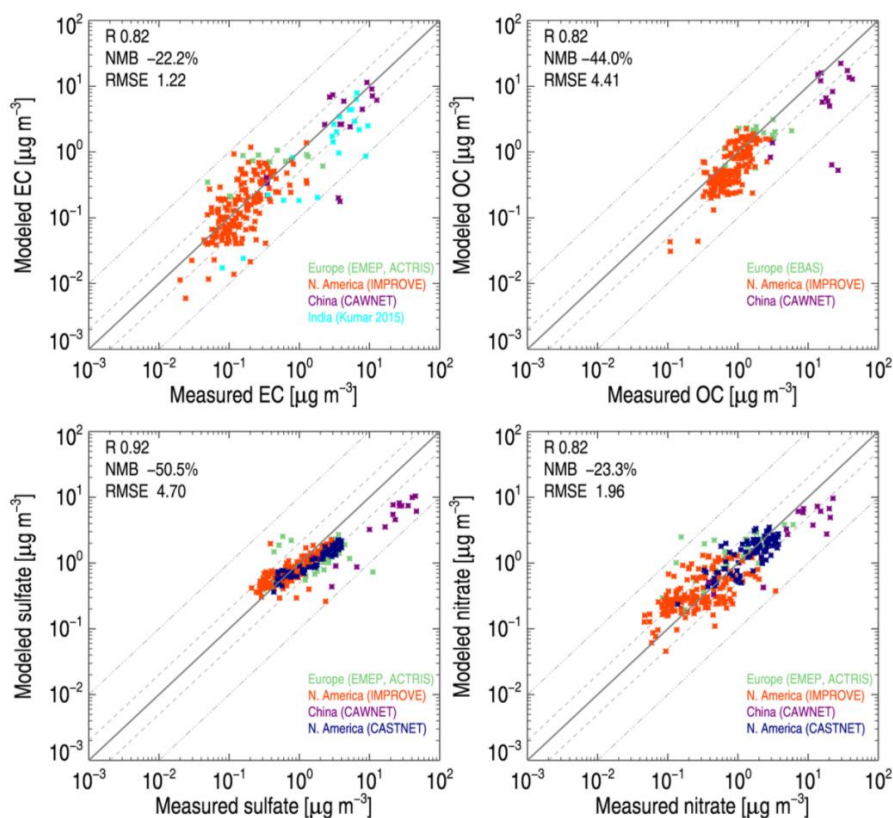
1258

1259

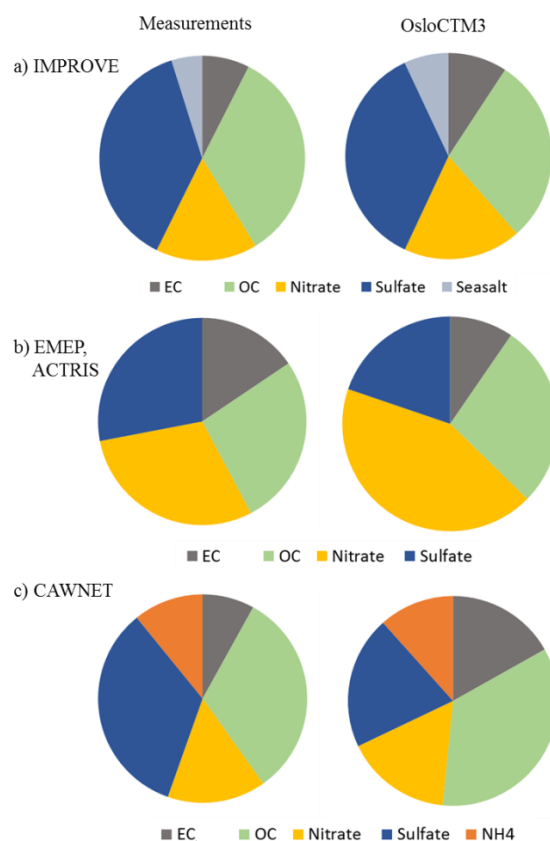
1260



1261
1262
1263 Figures



1264
1265
1266 *Figure 1: Annual mean modeled versus measured aerosol surface concentrations of a) EC, b)*
1267 *OC, c) sulfate and d) nitrate from the IMPROVE, EMEP, ACTRIS, CASTNET and CAWNET*
1268 *measurements networks.*



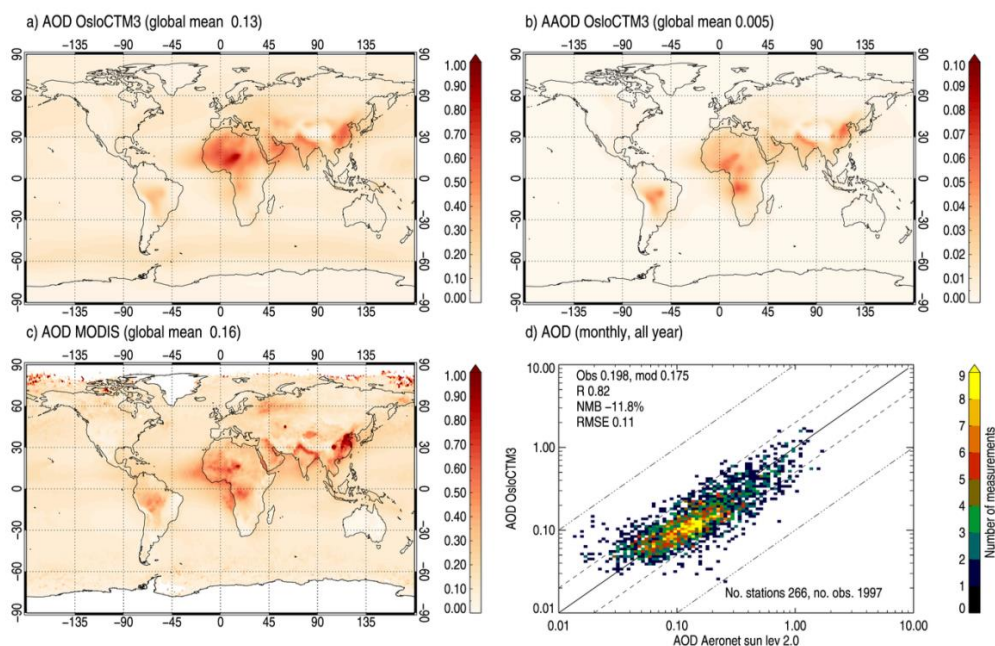
1269

1270

1271 *Figure 2: Aerosol composition (fraction of total aerosol mass) derived from the IMPROVE, EMEP,*
1272 *ACTRIS and CAWNET networks (left column) and corresponding OsloCTM3 results (right*
1273 *column).*

1274

1275



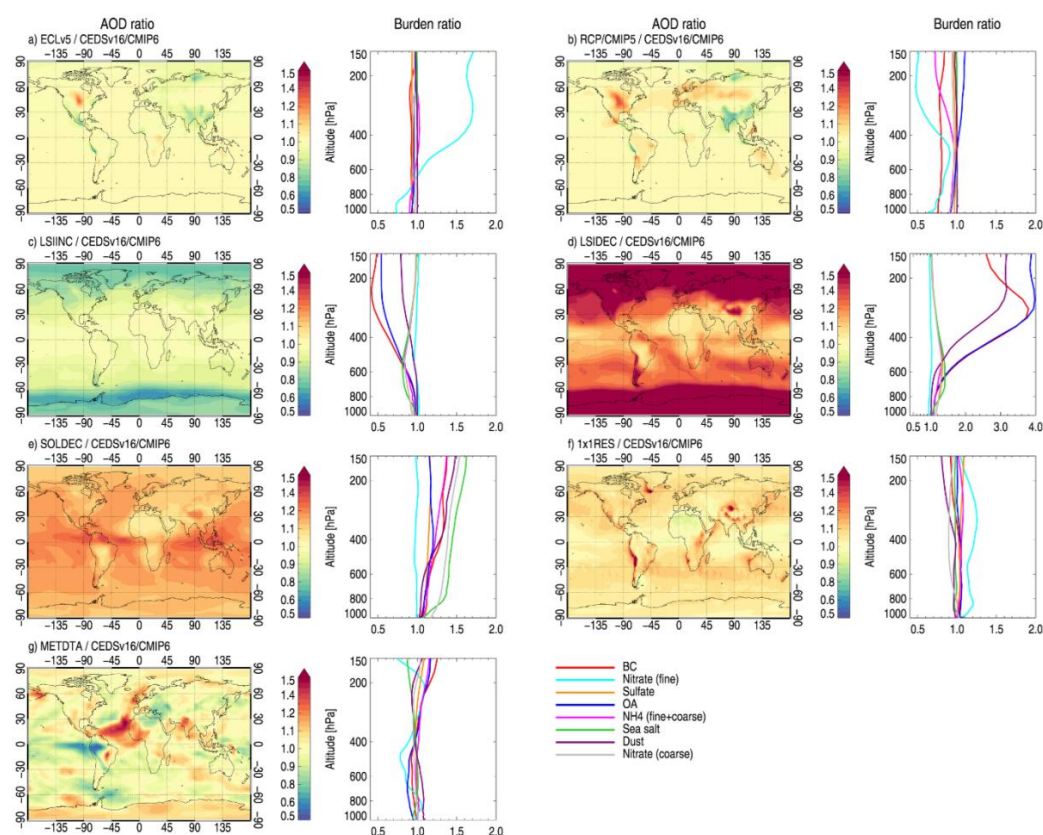
1276

1277 *Figure 3: Annual mean (year 2010) modeled a) AOD and b) AAOD, c) MODIS-Aqua AOD*
 1278 *retrieval and d) scatter density plot of comparison of simulated AOD against monthly mean*
 1279 *AERONET observations.*

1280

1281

1282

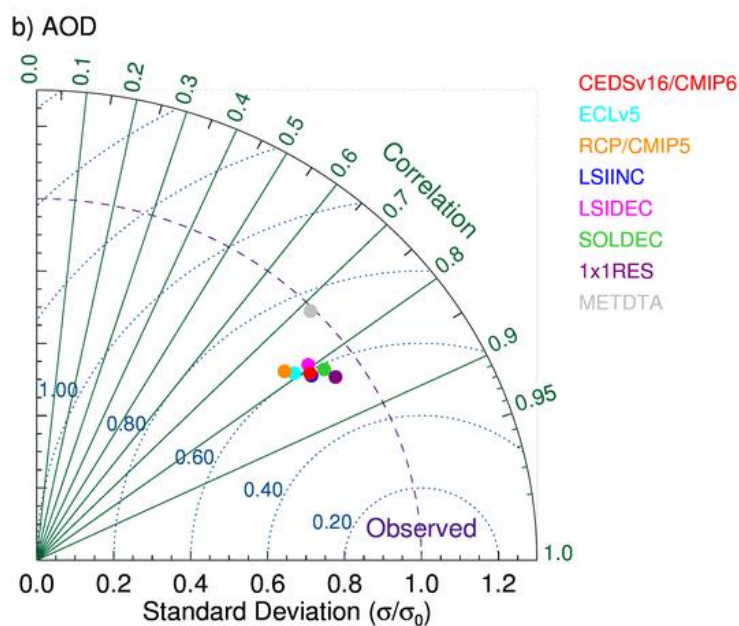
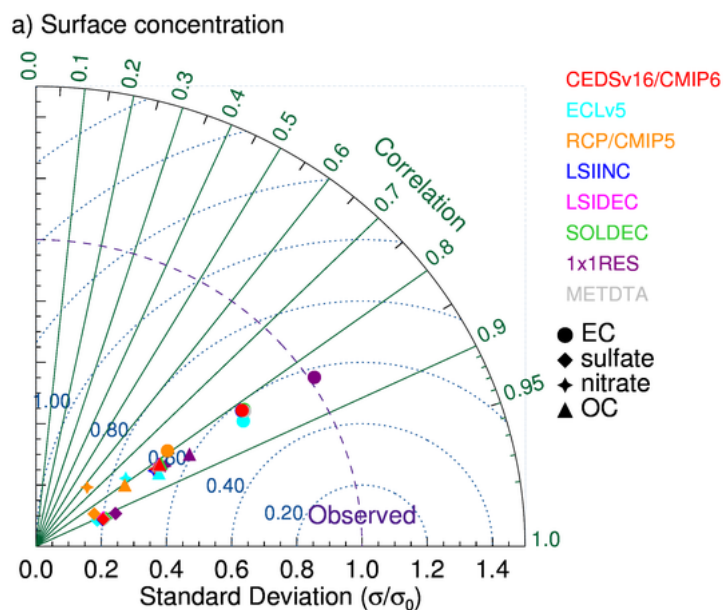


1283

1284 *Figure 4: Ratio of each sensitivity simulation relative to the baseline for AOD (columns 1 and 3)*
 1285 *and total burden by species in each model layer (columns 2 and 4).*

1286

1287

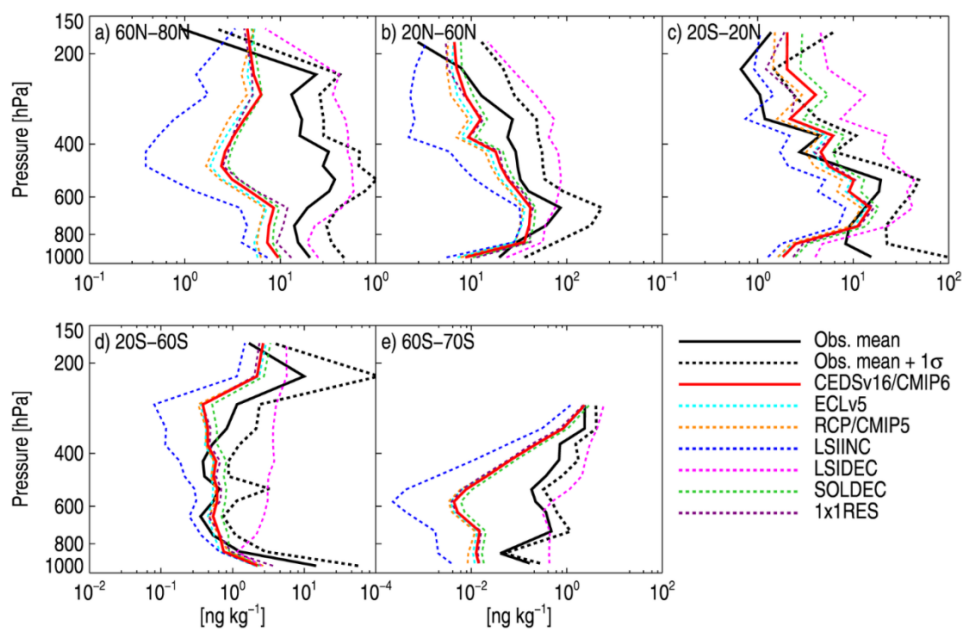


1290 *Figure 5: Taylor diagram of modeled and measured aerosol surface concentrations in the baseline*
 1291 *sensitivity tests using all observations in Fig. 1.*

1292
 1293



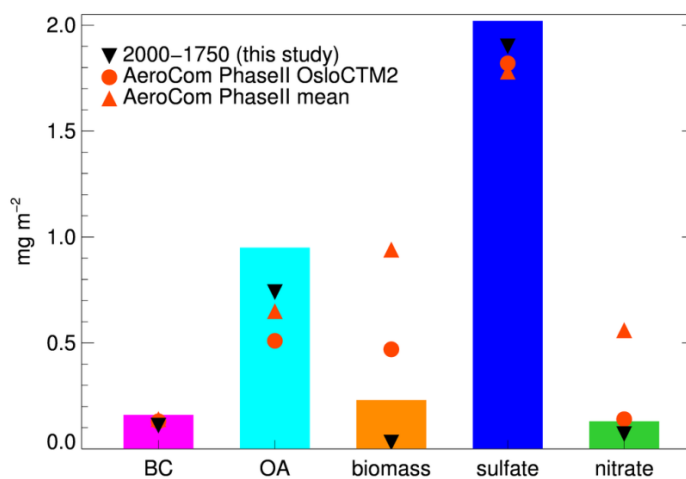
1294
1295
1296
1297
1298



1299

1300 *Figure 6: Modeled vertical BC profiles against rBC aircraft measurements in five different*
 1301 *latitudes bands over the Pacific Ocean from the HIPPO3 flight campaign. Model data is extracted*
 1302 *along the flight track using an online flight simulator. Black lines: mean of observations (solid),*
 1303 *mean + plus 1 standard deviation (dashed). Colored lines: OsloCTM3 baseline (CEDSV16/CMIP6)*
 1304 *(solid), sensitivity simulations (dashed).*

1305
1306
1307



1308

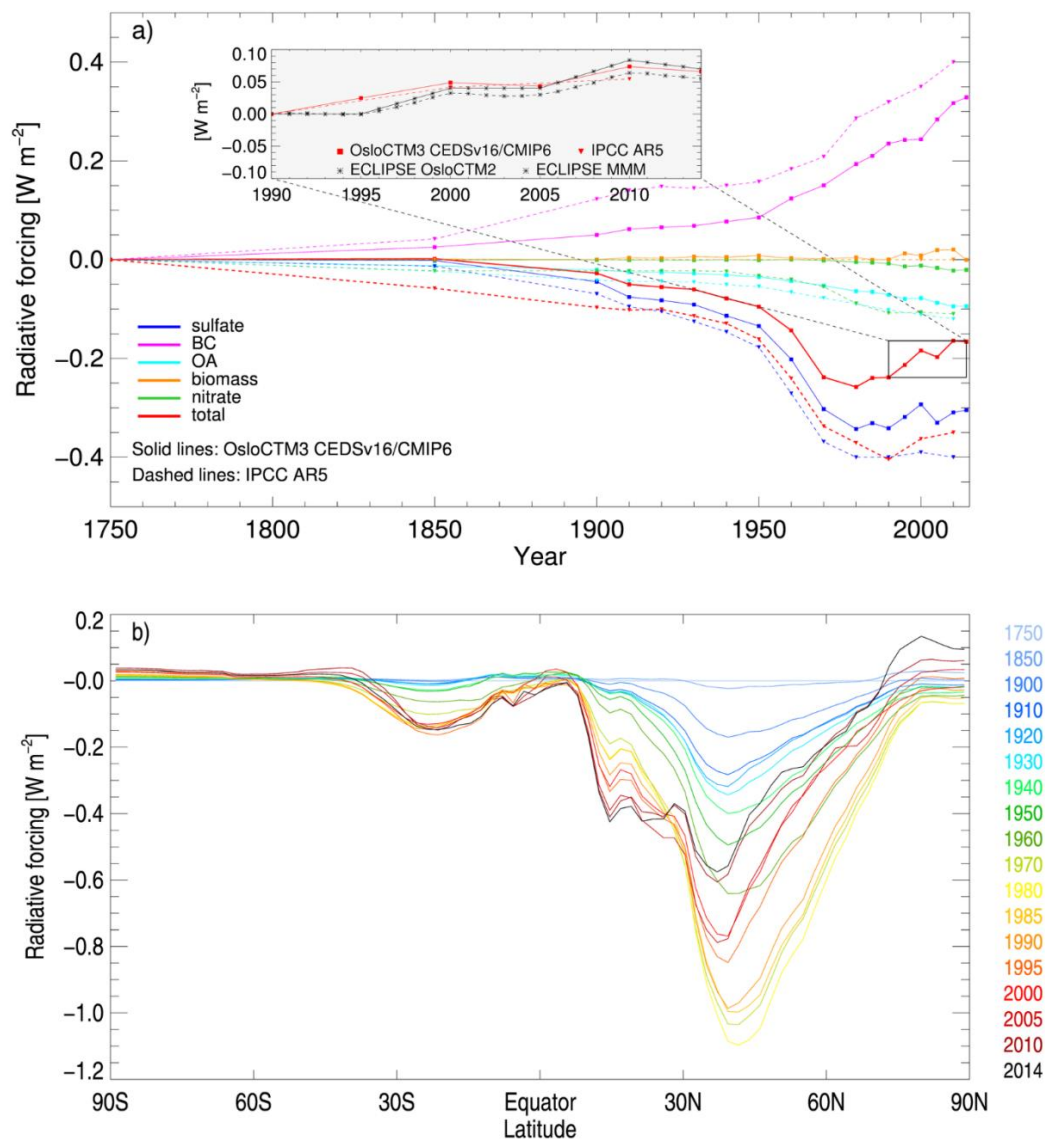
1309 *Figure 7: Change in anthropogenic aerosol load over the period 1750 to 2014 using CEDSv16*
 1310 *emissions. Black symbols show the 1750 to 2000 difference and red symbols show multi-model*
 1311 *mean and OsloCTM2 results from the AeroCom II experiments [Myhre et al., 2013a].*

1312

1313

1314

1315



1316

1317 *Figure 8: a) Time evolution of R_{Fari} . Solid lines show OsloCTM3 results from the current study,*
 1318 *while dashed lines show results from IPCC AR5 [Myhre et al., 2013b]. The inset shows the change*
 1319 *in total R_{Fari} between 1990 and 2015 in the current study compared with IPCC AR5 and multi-*



1320 *model mean and OsloCTM2 results from Myhre et al. [2017] using ECLv5 emissions. b) zonal*
1321 *mean RFari 1750-2014.*

1322